ORO-5135-77/7

THE EFFECTS OF FLOW CURVATURE ON THE AERODYNAMICS OF DARRIEUS WIND TURBINES

By
P. G. Migliore
W. P. Wolfe

July 1980

Work Performed Under Contract No. AC05-76ET20372

Department of Aerospace Engineering
West Virginia University
Morgantown, West Virginia

U.S. Department of Energy

Solar Energy

DISCLAIMER

DISCLAIMER

Available from the National Technical Information Service, U. S. Department of Commerce, Springfield, Virginia 22161.

Price: Paper Copy $9.00
Microfiche $3.50

ORO-5135-77/7
Distribution Category UC-60

THE EFFECTS OF FLOW CURVATURE ON THE AERODYNAMICS OF DARRIEUS WIND TURBINES

P. G. Migliore
W. P. Wolfe

Department of Aerospace Engineering
West Virginia University
Morgantown, West Virginia 26506

July, 1980

PREPARED FOR THE UNITED STATES
DEPARTMENT OF ENERGY
DIVISION OF SOLAR ENERGY
UNDER CONTRACT NO. EY-76-C-05-5135

THIS PAGE

WAS INTENTIONALLY

LEFT BLANK

ABSTRACT

A theoretical and experimental investigation was conducted which clearly showed the effects of flow curvature to be significant determinants of Darrieus turbine blade aerodynamics; qualitatively, these results apply equally to straight or curved bladed machines. Unusually large boundary layer radial pressure gradients and virtually altered camber and incidence are the phenomena of primary importance. Conformal mapping techniques were developed which transform the geometric turbine airfoils in curved flow to their virtual equivalents in rectilinear flow, thereby permitting the more accurate selection of airfoil aerodynamic coefficients from published sectional data. It is demonstrated that once the flow idiosyncracies are fully understood, they may be used to advantage to improve the wind energy extraction efficiency of these machines.

FOREWORD AND ACKNOWLEDGMENTS

The information presented herein addresses one particular aspect of the research conducted by the Department of Aerospace Engineering at West Virginia University. It deals specifically with the idiosyncratic aerodynamics associated with flow curvature and the resulting effects on the performance of Darrieus wind turbines. The report was prepared under DOE Contract Number EY-76-C-05-5135. Contributions of the following wind turbine project team members are gratefully acknowledged:

J. B. Fanucci	K. D. Kuhlke
R. E. Walters	C. C. White
G. M. Palmer	L. R. Metheney
C. D. Fries	S. B. Moore
S. K. Strimel	D. G. Elko

Editor's Note: Administration of this continuing project was transferred from D.O.E. to the Solar Energy Research Institute (SERI), Golden, Colorado, in 1978. Dr. Irwin Vas, SERI Program Manager, provided the final approval for this research report. Dr. Richard E. Walters, Project Principal Investigator at West Virginia University, was the report editor.

CONTENTS

FIGURES

TABLES

SYMBOLS AND NOMENCLATURE

ROMAN LETTERS	DEFINITION	METRIC UNITS	ENGLISH UNITS
ÆR	Turbine blade aspect ratio; ÆR = b/C		
b	Turbine blade span	m	ft
C	Turbine blade chord	cm	in
C/R	Flow curvature index		
C_D	Drag coefficient		
C_{D_e}	Effective drag coefficient		
$C_{D_{min}}$	Minimum drag coefficient		
C_L	Lift coefficient		
C_M	Moment coefficient		
C_P	Power coefficient; $C_P = T\omega/\rho V_\infty^3 bR$		
D	Drag per unit span; $D = \frac{1}{2}\rho V_R^2 C_D C$	N/m	lbf/ft
e	Oswald's planform efficiency factor		
Fr	Froude number		
L	Lift per unit span; $L = \frac{1}{2}\rho V_R^2 C_L C$	N/m	lbf/ft
M	Moment per unit span; $M = \frac{1}{2}\rho V_R^2 C_M C^2$	N	lbf
nb	Number of turbine blades		
R	Turbine radius	m	ft
Re	Reynolds number		
t	Time	s	s
T	Turbine rotor torque	N·m	ft·lbf
T_B	Turbine blade torque	N·m	ft·lbf
T_T	Turbine rotor support structure torque	N·m	ft·lbf
TSR	Turbine blade tip speed ratio		

ROMAN LETTERS	DEFINITION	METRIC UNITS	ENGLISH UNITS
V_R	Relative inflow velocity	m/s	ft/s
V_∞	Freestream wind velocity	m/s	ft/s
y_c	Maximum camber; i.e., the maximum distance from the airfoil chord to the mean camber line	cm	in
GREEK LETTERS			
α	Blade angle of attack with respect to relative inflow velocity	deg	deg
α_B	Blade pitch angle measured from turbine radius vector	deg	deg
β	Angle between the freestream wind and a perpendicular to the relative inflow velocity	deg	deg
α_g	"Geometric" angle of attack; the angle between the relative inflow velocity and the blade chord at the reference blade mounting point for the rotating blade	deg	deg
α_i	Effective angle of incidence resulting from flow curvature	deg	deg
α_v	"Virtual" angle of attack; the angle between the relative inflow velocity and the blade chord for the transformed airfoil in rectilinear flow: $\alpha_v = \alpha_g + \alpha_i$	deg	deg
ε	Inverse of the tip speed ratio		
θ	Angle between free stream wind and radius vector	deg	deg
ρ	Fluid mass density assumed everywhere equal to that of the free stream in the far field	kg/m^3	$slugs/ft^3$
σ	Turbine solidity; $nb/(2C/R)$		
ω	Turbine rotational speed	rad/s	rad/s

1. Introduction

Since 1975, the Department of Aerospace Engineering at West Virginia University (WVU) has conducted parallel experimental and analytical studies on straight bladed Darrieus wind turbines. This research, which was sponsored by the National Science Foundation, the Energy Research and Development Administration and the Department of Energy (DOE), had as its primary objective the evaluation of circulation controlled airfoils for more cost effective wind energy extraction. A prerequisite to that effort was a better understanding of the fundamental aerodynamics of Darrieus turbines, and the preliminary research directed toward that end revealed an aerodynamic complexity beyond initial expectations. The original research was to be purely analytical and directed toward developing reliable cost and performance models. But the dearth of reliable data for comparison became apparent rather quickly, and it was decided to construct the outdoor test model, shown in Figure 1, which would provide first hand cost and performance data.

The WVU turbine was not intended to be a prototype machine, but simply an aerodynamic test device which would permit the deduction of turbine blade drag coefficient, C_D, and wind energy extraction efficiency (power coefficient, C_p). In addition to the blade pitch schedule and turbine tip speed ratio (TSR), it was known that the blade aerodynamic drag and rotor solidity (σ) were primary determinants of C_p. By testing blades of different chord to turbine

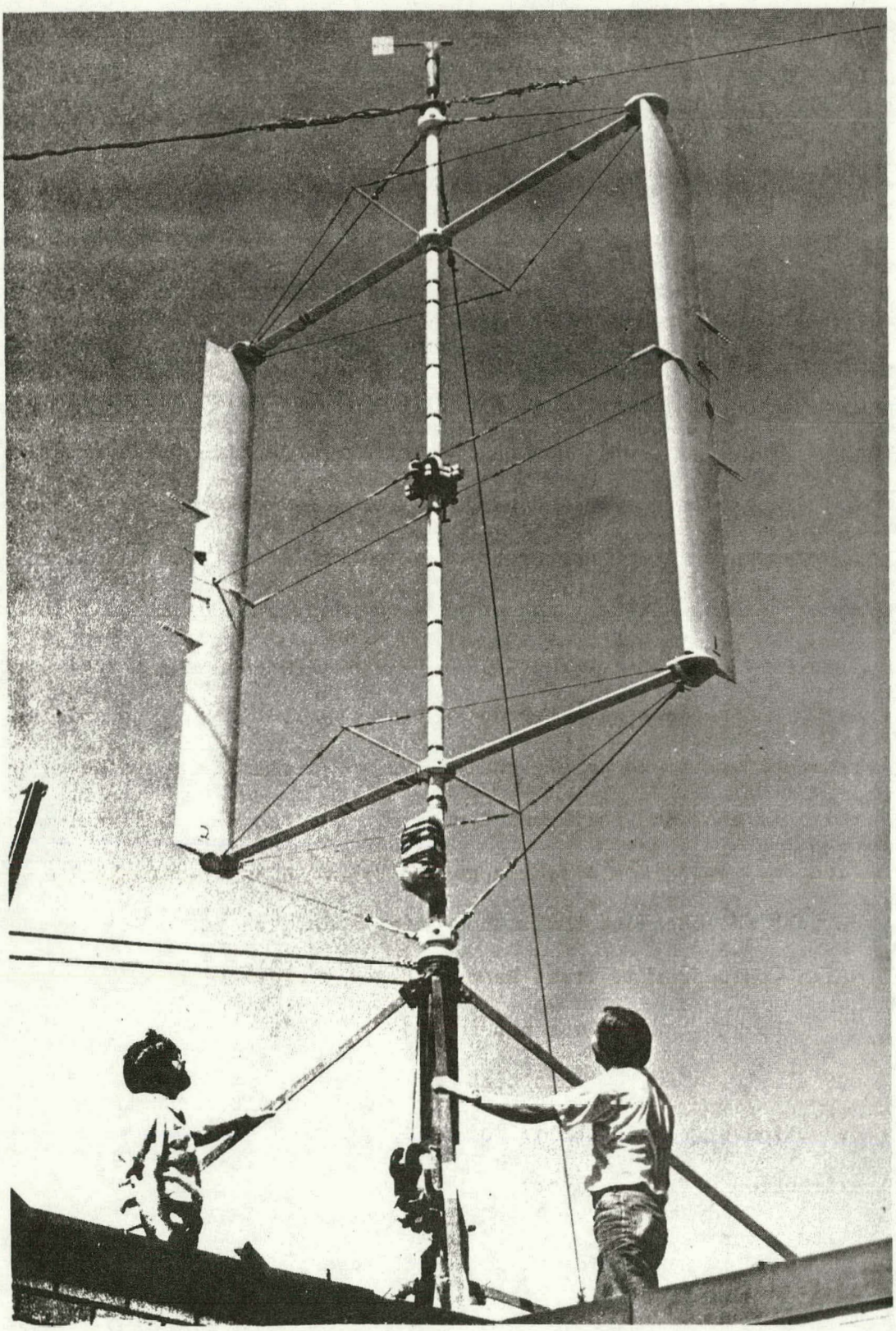

Figure 1. The WVU straight bladed Darrieus turbine outdoor test model.

radius ratio both σ and C/R could be varied and the effects observed (since C_D varies with Re and Re is a function of C/R). Therefore, two different sets of blades, both of NACA 0015 airfoil section, were tested. The first, nominally called the "small" blades, had a chord of 17.4 cm and C/R of 0.114; the second, called the "large" blades, had a chord of 39.7 cm and C/R = 0.260. Details of turbine design, test procedures and analysis of results appear in References 1, 2 and 3 respectively.

2. Experimental Tests

The small blade tests, designed to determine C_p for $\alpha_B = 90°$, gave the results shown in Figure 2. It was expected that different C_p curves would result for the different turbine rotational speeds, since C_p is strongly dependent on C_D, which in turn depends on Re and ω. However, no discernible pattern was obvious from Figure 2, and it was hoped that detailed drag investigations would offer additional insight. Test procedures had been developed which permitted deduction of blade C_D from measurements of torque for conditions of zero wind speed and no induced velocities. Figure 3 shows that with these assumptions the blade lift acts along the turbine radius arm and produces no torque. The drag and moment, if it exists, produce countertorque which will depend upon ω and α. The situation is mathematically modeled as follows. (Refer to Figure 3.a for detailed geometry.)

The instantaneous torque, T_B, produced by a single turbine blade depends upon its orbital position, θ, and is given by

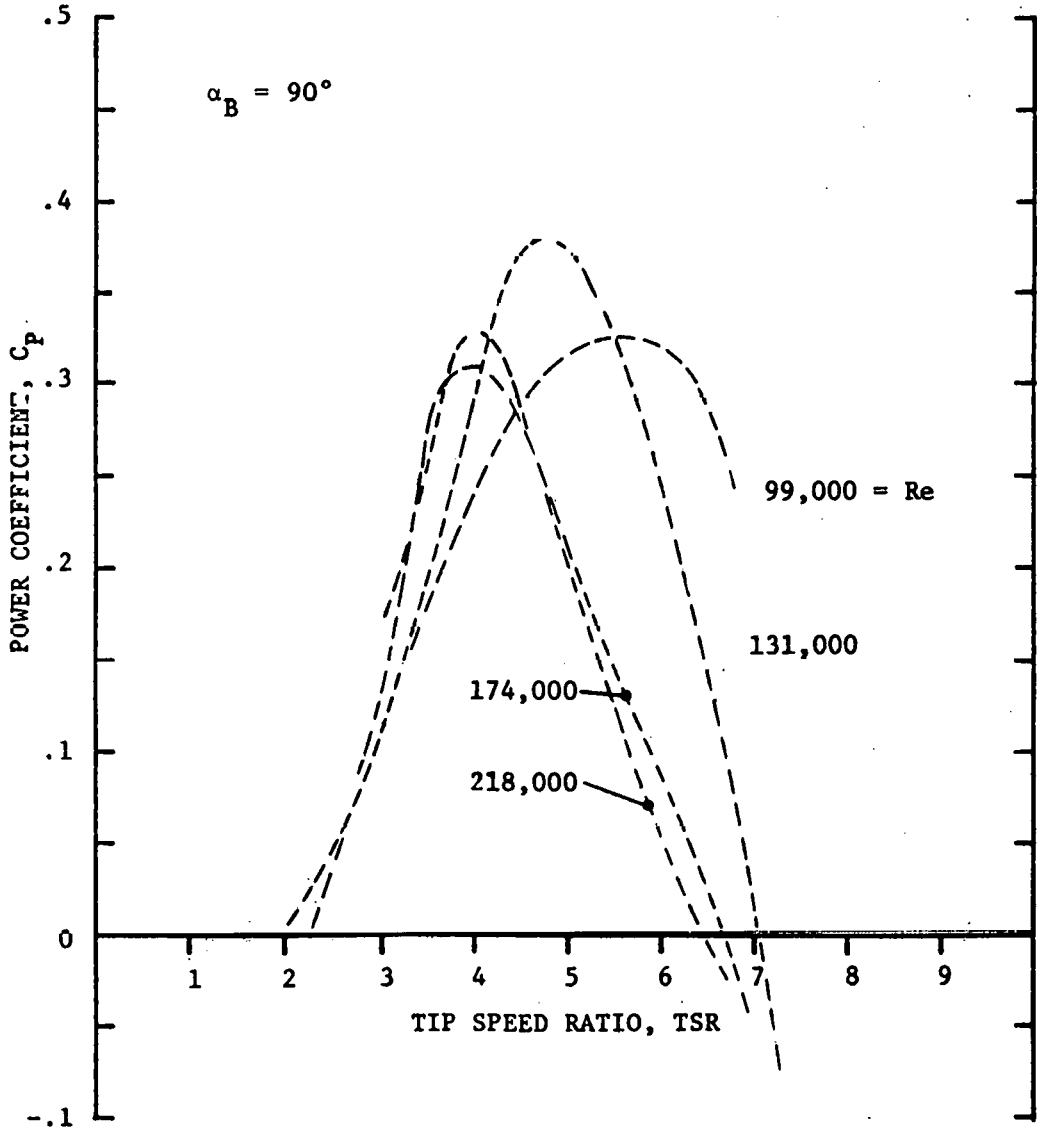

Figure 2. Experimentally determined power coefficient for small blades(C/R = .114, AR = 18.7)

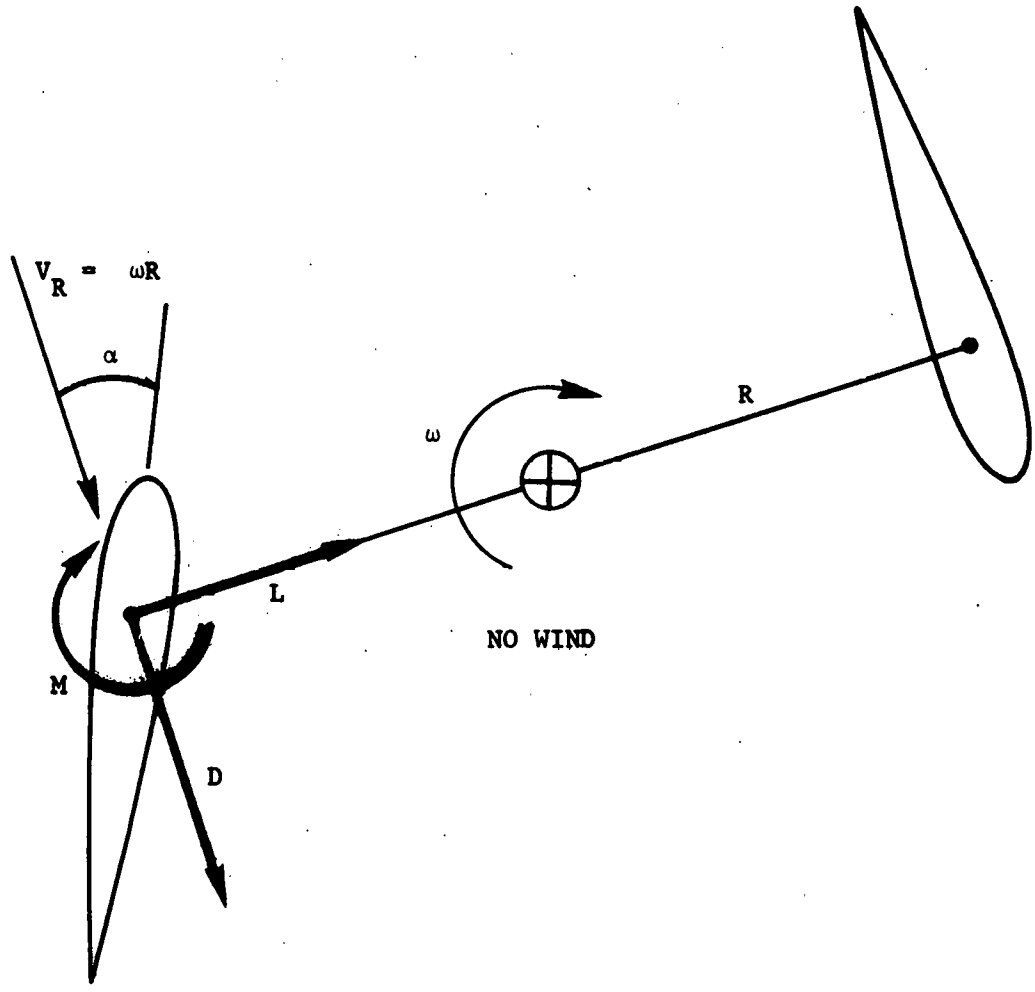

Figure 3. Aerodynamic forces at zero wind conditions

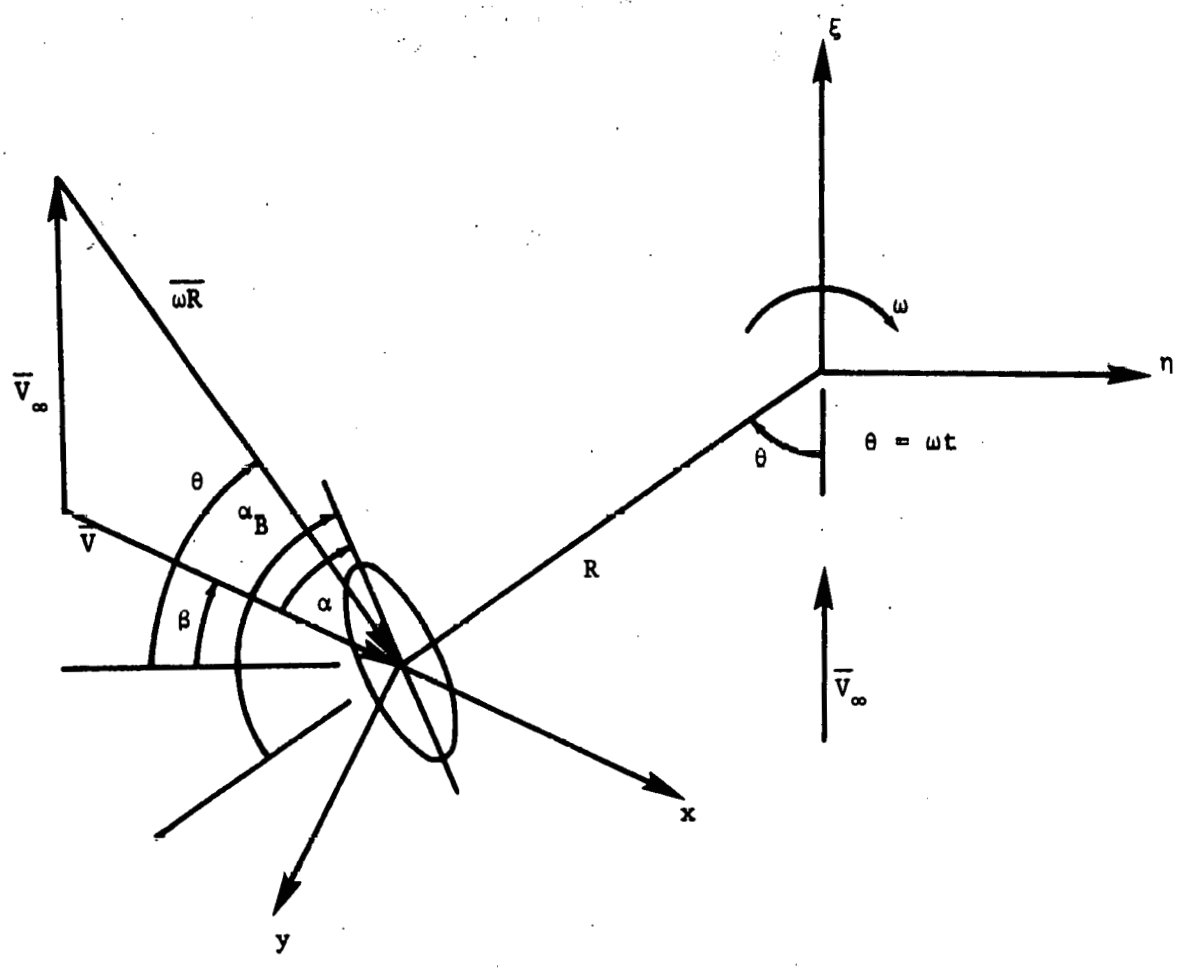

Figure 3.a. Geometry for mathematical analysis of turbine

$$T_B(\theta) = \tfrac{1}{2}\rho V_R^2 \, CbR \left[C_L \sin(\theta-\beta) - C_D \cos(\theta-\beta) + C_M \, C/R \right] . \quad (1)$$

The difference, $\theta - \beta$, is the angle of inclination of the lift vector to the turbine radius arm, and for the assumed conditions is always equal to zero. C_M is the blade aerodynamic moment coefficient about the point of attachment to the support arm. V_R is the blade relative inflow velocity, which for zero wind is constant and equal to ωR. Since V_R and α are constant, so is $T_B(\theta)$, and Equation 1 may be written as

$$T_B = \tfrac{1}{2}\rho\omega^2 R^3 \, Cb \, [-C_D + C_M \, C/R] . \quad (2)$$

Since the WVU turbine has two blades the total torque produced is

$$T_B = k \, [- C_D + C_M \, C/R], \quad (3)$$

where $k = \rho\omega^2 R^3 \, Cb$ (4)

is a function only of atmospheric conditions and the turbine RPM. Since the turbine blades were mounted at their quarter chord, and for symmetrical airfoils C_M about this point is zero, the blade drag coefficient from Equation 3 is

$$C_D = -T_B/k . \quad (5)$$

The blade torque, T_B, is deduced [2,3] from the measured turbine torque T and the known support structure tare torque, T_T, under the previously assumed conditions. That is,

$$T_B = T - T_T \quad , \tag{6}$$

and will of course always be negative. In the general case where C_M is not zero, Equation 3 for the blade drag becomes more complicated, as shown in Equation 7:

$$C_D = \frac{-T_B}{k} + C_M \, c/R \quad . \tag{7}$$

In order to deduce C_D from this equation, C_M must be known, and this is unlikely. It is much more useful to define an effective drag coefficient, C_{D_e}, which combines the net detrimental effects of aerodynamic drag and moment to produce countertorque. By definition and analogy to Equation 5 this effective drag is given by

$$C_{D_e} = -T_B/k \quad . \tag{8}$$

C_{D_e} will always be greater than C_D if the turbine blade produces a nose out pitching moment. In this report, C_D and C_{D_e} will be used interchangeably unless there is some reason to distinguish the two.

Applying the above analysis to the test results for the small blades gives the effective drag curves of Figure 4. These are referred to as drag polars although they plot C_D versus α, instead of versus C_L. The plots result from torque data at different blade pitch settings where α is known, but C_L is not known since test instrumentation was not designed to measure C_L. The α versus C_D curves

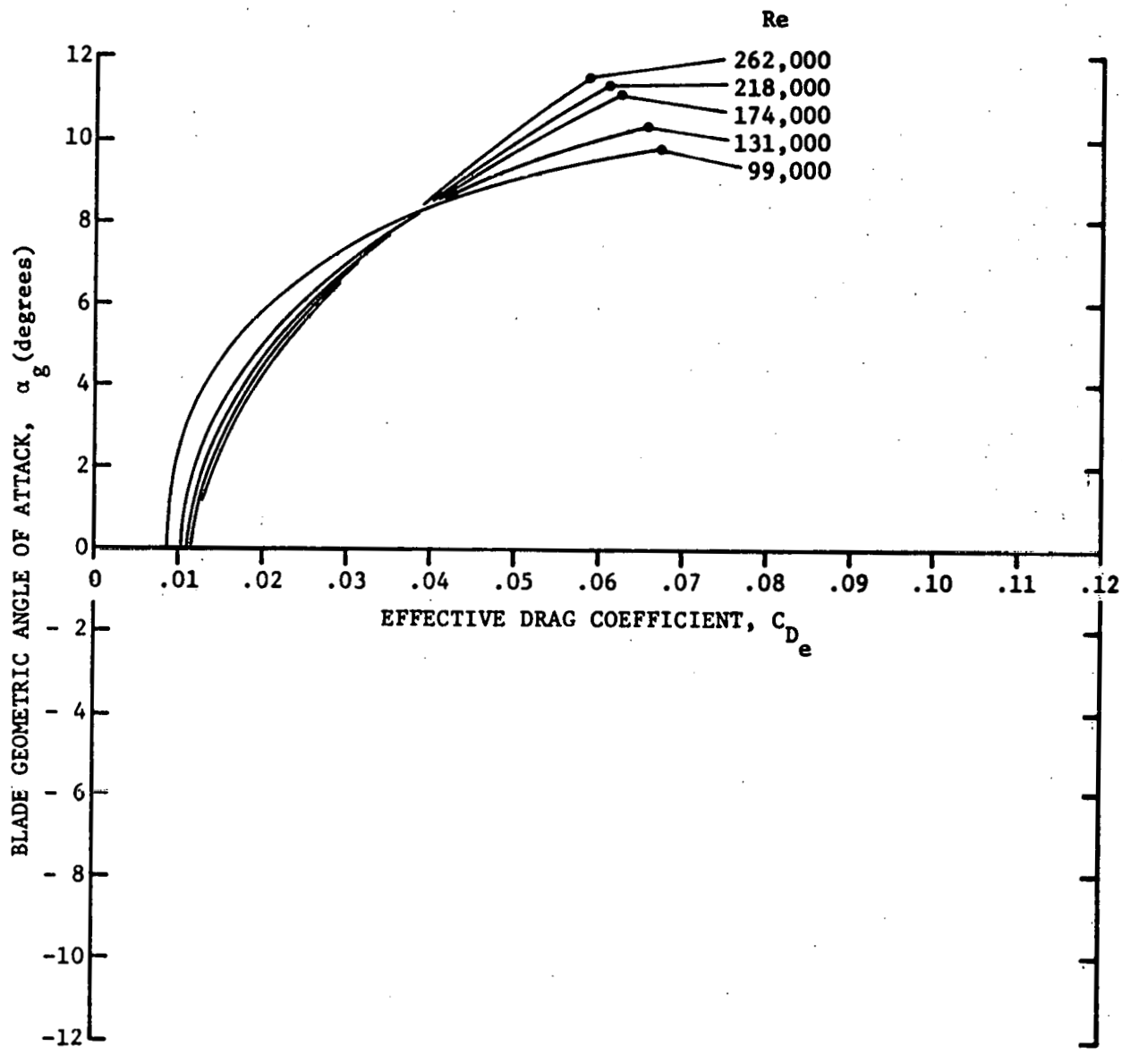

Figure 4. Experimentally determined drag polars (C_{D_e} vs α_g) for small blades (C/R = .114, AR = 18.7)

provide the same qualitative information as C_L versus C_D since the C_L-α relationship is nearly linear in the test range. There were two curious features noted when Figure 4 was plotted. First, at $\alpha = 0$ (which presumably corresponds to $C_L = 0$), C_D increases with increasing Reynolds number. This is contrary to the normally observed trend over the range of test Re. Secondly, the minimum drag coefficient, $C_{D_{min}}$, appeared to occur at negative angle of attack, α_g, a characteristic indicative of non-zero airfoil incidence, camber, or both. These two observations were perplexing and prompted various efforts to more adequately interpret the phenomena.

A theoretical boundary layer analysis [4,5] by Fanucci showed that the orbital motion of the turbine blades resulted in extraordinary normal pressure gradients which could appreciably influence both lift and drag. In the continuing discussion, these boundary layer properties are referred to as "centrifugal effects." At the same time, some unpublished research at WVU and the more formal studies of Wolfe [3,6] showed that the usual assumptions of constant V_R and α over the entire blade chord could introduce substantial error in blade aerodynamic analysis. These findings differed from those of Muraca [7] at NASA, who concluded that the effects of flow curvature could be neglected for (small) $\bar{C}/\bar{R}$ on the order of 0.10. Fortunately, the experimental test program at WVU offered the opportunity to substantiate the predicted overall detrimental effects of flow curvature. Analysis showed that these effects

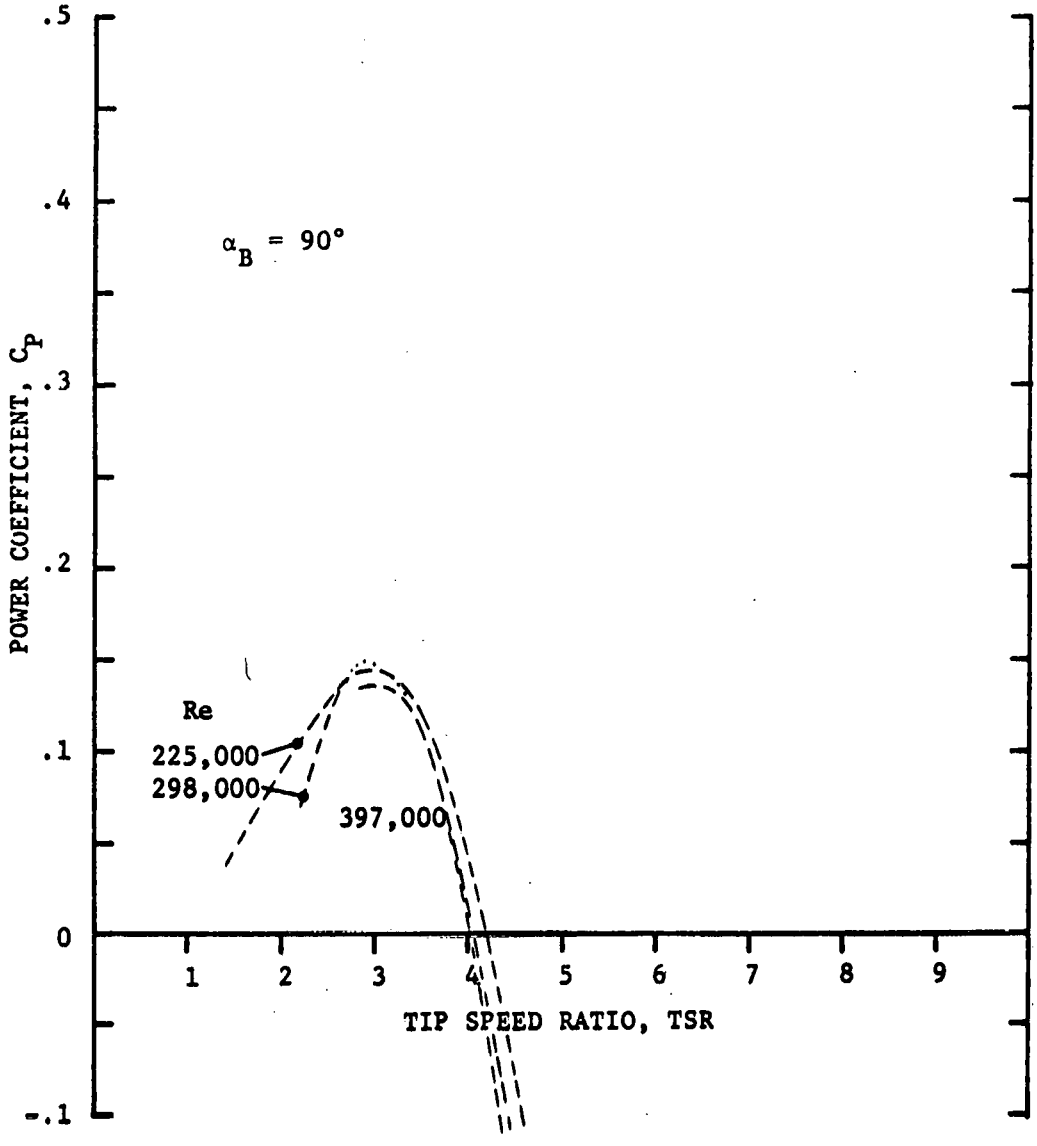

Figure 5. Experimentally determined power coefficient for large blades (C/R = .260, AR = 8.2)

should be even more pronounced for the large blades of C/R = .26. Indeed, the large blade test results (Figure 5) show a marked decrease in power coefficient compared to the small blade results (Figure 2). Similarly, the large blade drag coefficient analysis (Figure 6), shows accentuated distortion of the drag polar as compared to the small blade results (Figure 4).

Before meaningful conclusions can be drawn from the data of Figures 4 and 6, the initial assumption of no induced velocities must be examined. For finite span blades, velocities will be induced as a by-product of lift production analogous to aircraft wind downwash. The effects will be similar, i.e., the true lift vector will be displaced from the blade support arm by an induced angle and the measured drag will contain a lift component. Without determination of the lift component magnitude, the measured C_{D_e} data lose quantitative meaning. Meaningful qualitative conclusions may be drawn, however, by considering general aerodynamic characteristics of symmetrical and cambered airfoils.

For a symmetrical airfoil section, $C_{D_{min}}$ occurs at $\alpha = 0$ and $C_L = 0$. Therefore, for any symmetrical blade, there will be no induced velocities at $\alpha = 0$ and $C_{D_{min}}$ will remain unchanged. For a cambered airfoil section, $C_{D_{min}}$ occurs at $\alpha \approx 0$ and positive C_L. Therefore, there will be induced velocities at $C_{D_{min}}$ and an increase in drag. This combination will tend to shift $C_{D_{min}}$ to a more negative angle where there is a smaller C_L and less induced drag.

From this analysis it is clear that if the VAWT blades were behaving as symmetrical airfoils, there would be no shift of $C_{D_{min}}$ away from $\alpha_G = 0$. The fact that there is a shift is conclusive proof that the VAWT blades are exhibiting cambered properties.

These results supported the hypothesis that flow curvature effects are important determinants of Darrieus turbine aerodynamics. The remainder of this report considers flow curvature in some detail.

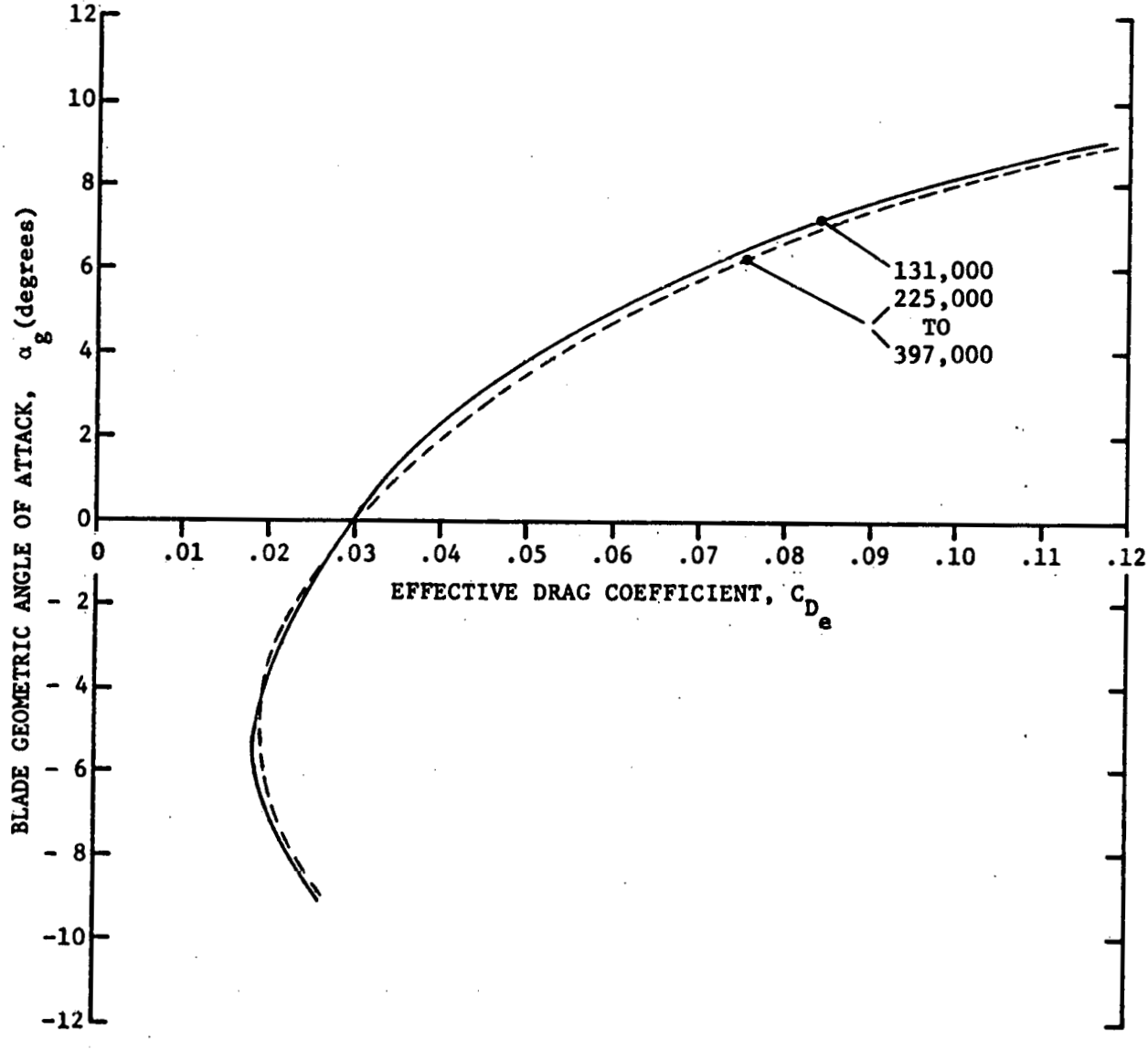

Figure 6. Experimentally determined drag polars (C_{D_e} vs α_g) for large blades (C/R = .260, AR = 8.2)

3. Some Important Flow Curvature Considerations

3.1 Dimensional Analysis

It is of interest to examine the relevant parameters which characterize the fluid dynamics of Darrieus turbines. The parameters that characterize the effects of external forces, viscosity, compressibility and heat transfer may be determined by dimensional analysis [8]. Compressibility and heat transfer are neglected and it is assumed that the aerodynamic force experienced by the turbine blades will depend on the following parameters*:

$$F = f(\rho, V, C, \mu, g, R) \tag{9}$$

where the symbols and their dimensions are as tabulated.

Symbol	Name	Dimensions**
F	Force	MLT^{-2}
ρ	Density	ML^{-3}
V	Blade relative inflow velocity, V_R	LT^{-1}
C	Characteristic length of the body (the blade chord)	L
μ	Coefficient of viscosity	$ML^{-1}T^{-1}$
g	Gravitational force on fluid element	LT^{-2}
R	Characteristic length of the turbine (the turbine radius)	L

*The blade rotational speed, ω, could also have been chosen, but it can be shown that the additional π product which results is superfluous.

**M = mass, L = length, T = time

Equation 9 is written in the following form:

$$h(F, \rho, V, C, \mu, g, R) = 0. \tag{10}$$

There are seven variables and three fundamental dimensions. Therefore, there are four dimensionless π products. Choosing (ρ, V, C) as an arbitrary set, the π products which result are

$$\pi_1 = f_1(F, \rho, V, C) , \tag{11}$$

$$\pi_2 = f_2(\mu, \rho, V, C) , \tag{12}$$

$$\pi_3 = f_3(g, \rho, V, C) , \tag{13}$$

and

$$\pi_4 = f_4(R, \rho, V, C) . \tag{14}$$

The dimensionless combinations of variables for the above π products are found to be

$$\pi_1 = \frac{F}{\rho V^2 C^2} , \tag{15}$$

$$\pi_2 = \frac{\rho VC}{\mu} , \tag{16}$$

$$\pi_3 = \frac{V}{\sqrt{gC}} , \tag{17}$$

and

$$\pi_4 = C/R . \tag{18}$$

Then Equation 10 may be written as

$$h\left(\frac{F}{\rho V^2 C^2} , \frac{\rho VC}{\mu} , \frac{V}{\sqrt{gC}} , \frac{C}{R}\right) = 0 . \tag{19}$$

The first term in the bracket of Equation 19 is the ratio of the total body force to the inertial force (the rate of change of momentum of a fluid element). The parameter is characteristic of all aerodynamic problems. The second term is the Reynolds number, Re, the ratio of inertial force to viscous force. Re influences turbine blade lift and drag. The third term is the Froude number, Fr, the ratio of inertial force to external (gravitational) force. The fourth term, C/R, may be unique to fluid dynamic problems where the body orbits a fixed point in space and the relative inflow velocity depends on the radius R. The authors have not encountered this term elsewhere in the literature, and for discussion purposes it is defined here as the "curvature index".

The importance of Fr and the curvature index will be noted in Sections 3.2, 3.3, and 3.4, respectively.

3.2 Centrifugal Effects

Fanucci [5] has shown that for Darrieus wind turbines, the normal pressure gradient through the blade boundary layer is at least an order of magnitude larger than that normally experienced in curved flows. In fact, the pressure gradient normal to the blade surface is proportional to the square of the tip speed ratio, TSR^2. Intuitively, one concludes that this strong radial pressure gradient may lead to premature laminar boundary layer separation with an attendant loss of lift and increase in drag. But the low

pressure surface of the airfoil varies cyclically with blade rotation, since α cyclically changes sign. Therefore, on the upstream side of the turbine, centrifugal effects might delay separation, while on the downstream side they will almost certainly accelerate separation. At the present, one can only speculate regarding the net effect on turbine performance.

An alternate approach to considering the importance of centrifugal effects is by examination of the relevant flow parameters Re and Fr. Re characterizes viscous effects which are obviously important. Froude number, Fr, characterizes external forces, the neglect of which are not obviously justifiable. Normally, gravity forces are the only external forces acting on the fluid. A fluid element of volume (dv) experiences a gravitational force of $\rho g(dv)$, where g is the acceleration of gravity. But owing to viscosity and the orbital motion of the blades, an additional "pseudo-gravitational" (centrifugal) force of approximately $\rho\omega^2 R(dv)$ is experienced, which can easily be an order of magnitude greater than $\rho\, g(dv)$. Froude number is given by the equation

$$Fr = \frac{V}{\sqrt{g\ell}} \quad , \qquad (20)$$

where the velocity V is taken to be the mean value of the blade relative inflow velocity, $V = \omega R$, and the characteristic length ℓ is the blade chord, C. Considering the centrifugal acceleration $\omega^2 R$, as being analogous to the gravitational acceleration, g, and substituting in Equation 20 gives

$$Fr = \sqrt{R/C} = \frac{1}{\sqrt{C/R}} \qquad (21)$$

The conditions for neglecting the effects of external forces [9] in comparison with inertial effects is that $Fr^2 >> 1$. Since C/R is typically small, this condition is satisfied. The condition for neglecting the effects of external forces in comparison with viscous effects is that $Fr^2/Re >> 1$, a condition which is clearly not met. Thus, there is further evidence that centrifugal effects must be considered in turbine aerodynamic analysis. It is difficult to see how these might be investigated analytically, and the present research does not consider them further. This decision was made on the basis of expediency, since time and money were scarce commodities. However, the authors have conceptually developed an experimental test program to investigate centrifugal effects. The method will be discussed in later sections of this report.

3.3 Kinematics

One of the simplifying assumptions in the analysis of Darrieus turbines has been that an average instantaneous blade relative inflow velocity and angle of attack could be accurately defined. These are normally assumed to be the values calculated at the point of attachment of the turbine blade to its support arm, a distance R from the turbine axis of rotation. Upon closer examination, however, it is found that this assumption may lead to errors. The question

arises, "Under what conditions are these errors negligible?"

The radial distance from the turbine axis of rotation to any point on the blade surface (or chord) is unique. Taking this "local" radius into proper consideration when defining the turbine geometry leads to a mathematical expression for the "local" angle of attack, α, and relative inflow velocity, V_R. These are derived in Appendix A. A typical chordwise variation of V_R and α is illustrated in Figure 7 for the airfoil used for the large blades tested on the WVU turbine. In this case the blade mounting point was at the quarter chord. Analysis shows that V_R changes along the chord, but only by a few percent. Figure 8 shows the change in α to be very large (at θ=90°), proceeding from -5° at the leading edge to +15° at the trailing edge. This V_R and α variation depends on the blade location relative to the free stream wind, θ, the tip speed ratio, TSR, and the curvature index, C/R. The cyclic variation of α with θ is illustrated in Figure 9 for a TSR typical of the optimum value for a straight bladed Darrieus turbine. The increment in α from leading to trailing edge varies somewhat, but is substantial over the entire orbit. It can also be shown that the effect becomes more pronounced as C/R increases.

From this simple kinematic analysis it is apparent that flow curvature markedly alters the relative velocity and angle of attack of the turbine blades. It is logical to conclude that the resulting aerodynamic properties will differ from those of blades in rectilinear flow. The variation in V_R and α is analogous to that

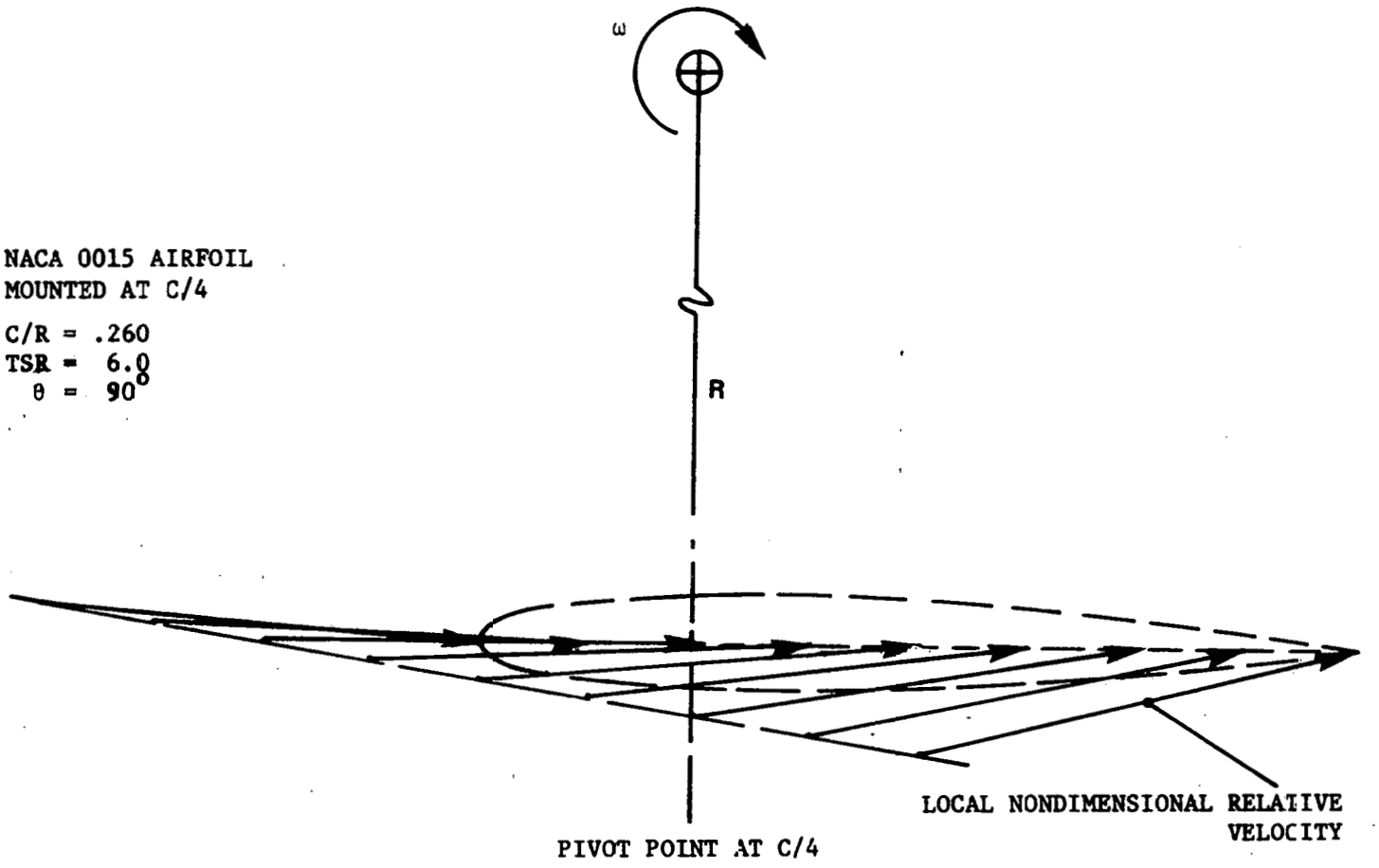

Figure 7. Example of the instantaneous local relative velocity distribution along the chord

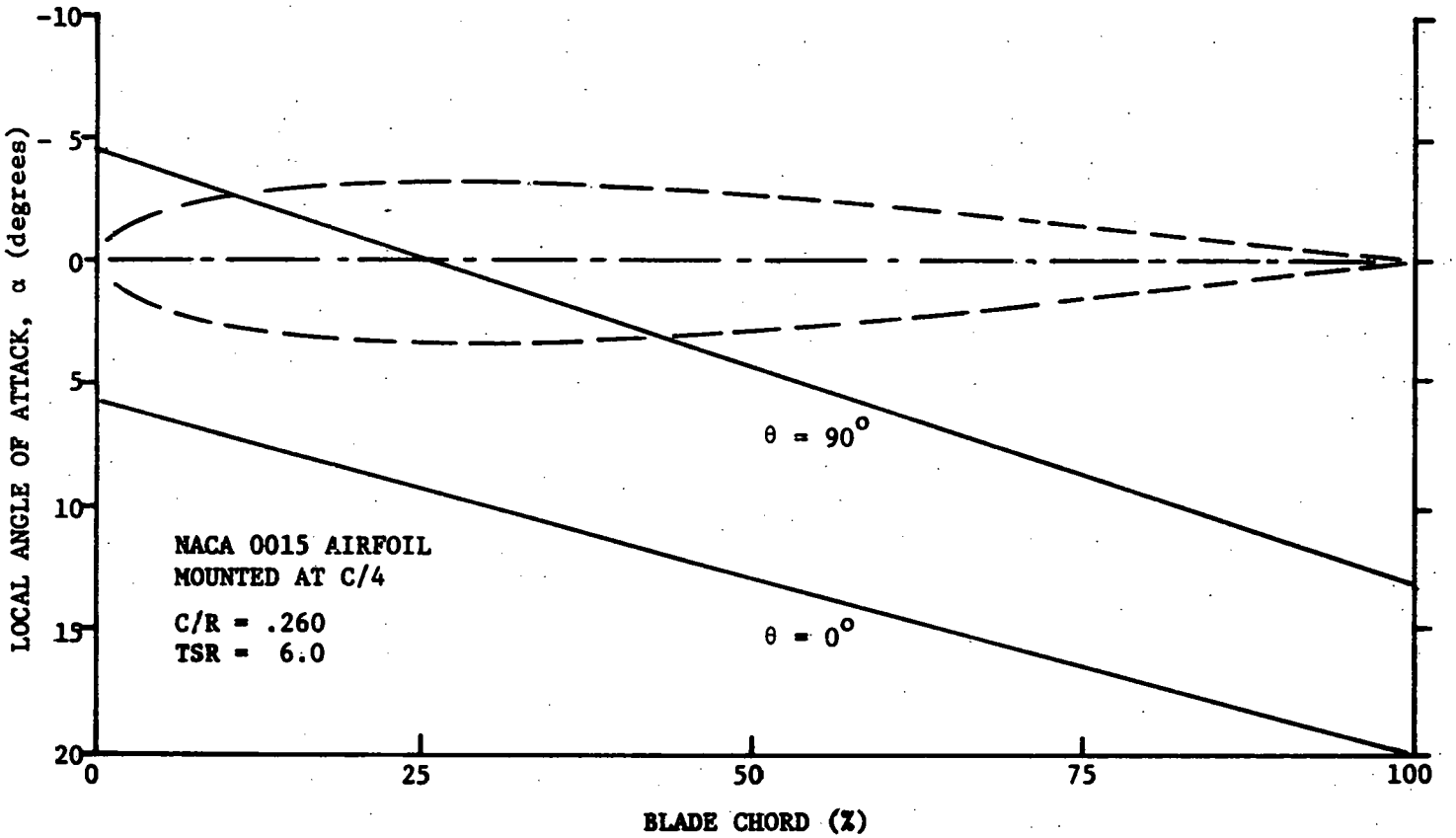

Figure 8. Variation of the local angle of attack from the leading to the trailing edge

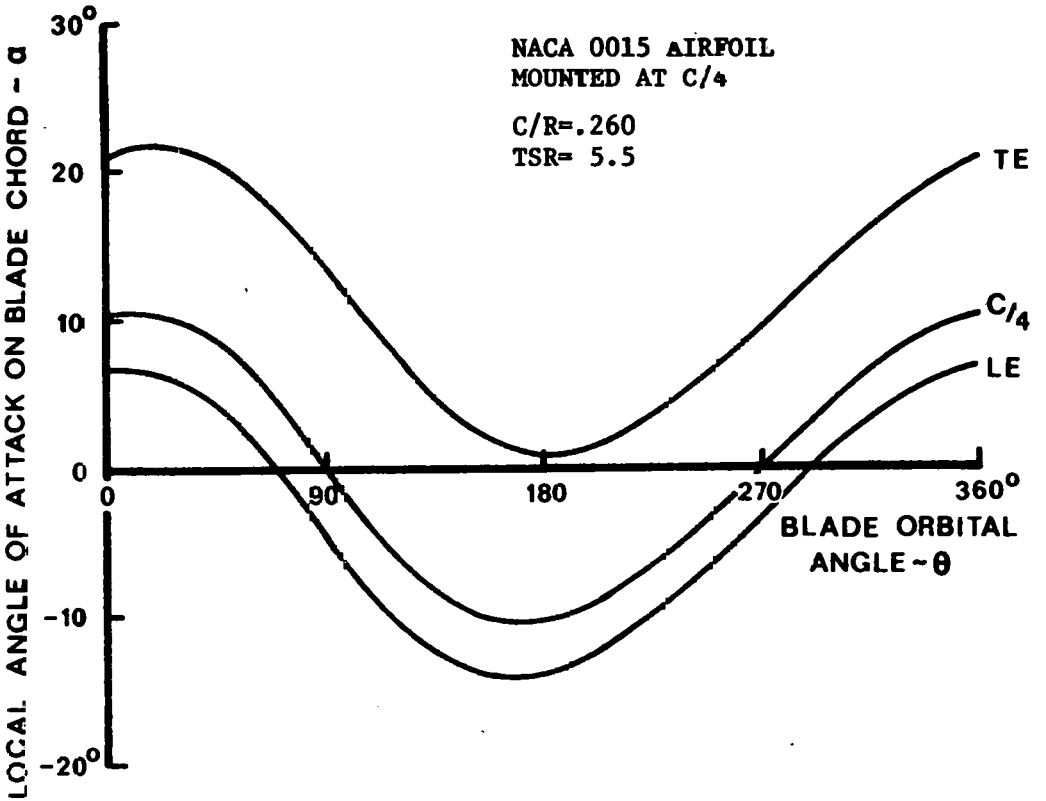

Figure 9. Typical variation of the local angle of attack on the blade chord.

experienced by cambered airfoils. This observation led to speculation that perhaps the symmetrical airfoils in curvilinear flow would exhibit the aerodynamics of cambered airfoils in rectilinear flow. This phenomenon had been noted by Muraca [7] and received subsequent review by Ashley [10], but was dismissed as insignificant for blades of small C/R. The WVU researchers were not similarly convinced, however, and so proceeded with the more detailed conformal mapping analysis which follows.

3.4 Conformal Mapping Analysis

The curvilinear flow field of Darrieus turbines may be examined with the aid of conformal mapping techniques. By this method [3], the actual (geometric) airfoil in the curved flow may be transformed to an equivalent (virtual*) airfoil in a rectilinear flow. By this approach, local velocities and angles of attack are preserved, so that the virtual airfoil should exhibit the aerodynamic behavior of the geometric airfoil in orbit. Sectional airfoil data is then applicable to the virtual airfoil.

Derivation of the transformation equations appears in Appendix B. The computer codes which implement the method are found in Appendix C. The influence of virtual camber on airfoil geometry is discussed in this section, while the impact on aerodynamics is treated in Section 4.

---

*This process effects a change in camber; thus the terminology "virtual camber" is applied to the airfoils which have a particular camber in essence but not in fact.

Figure 10 illustrates the transformation procedure for an NACA 0015 airfoil typical of those chosen for Darrieus turbines. Properties of the virtual airfoil vary with the assumed C/R, θ, and TSR. For the present case, the symmetrical airfoil was assumed to be mounted at its quarter chord at zero angle of incidence ($\alpha_B = 90°$) to the rectilinear blade velocity vector. It was further assumed that the free stream wind was zero (TSR = ∞), and thus, dependence on orbital position, θ, was removed. This rather simplistic assumption in no way invalidates the qualitative illustration of virtual camber effects. Analysis shows that flow curvature introduces an effective angle of incidence in addition to the normal blade angle of attack; airfoil camber is also altered. Since the magnitude of both are strongly dependent on C/R, Figure 11 reflects this functional relationship. Of particular interest are the results for the small and large blades tested on the WVU turbine. It was found that the small blades (C/R = .114) transform to airfoils having 1.4% camber and 1.6° incidence, and the large blades (C/R = 0.260) transform to airfoils having 3.2% camber and 3.7° incidence.

3.5 Cyclic Reynolds Number Variation

At low and moderate Re, where Darrieus turbines typically operate, blade aerodynamics are strongly influenced by Re. Lift curve slope, stall angle, and minimum drag coefficient, $C_{D_{min}}$, are all sensitive to Re. Owing to the variation of V_R with orbital position, a cyclic

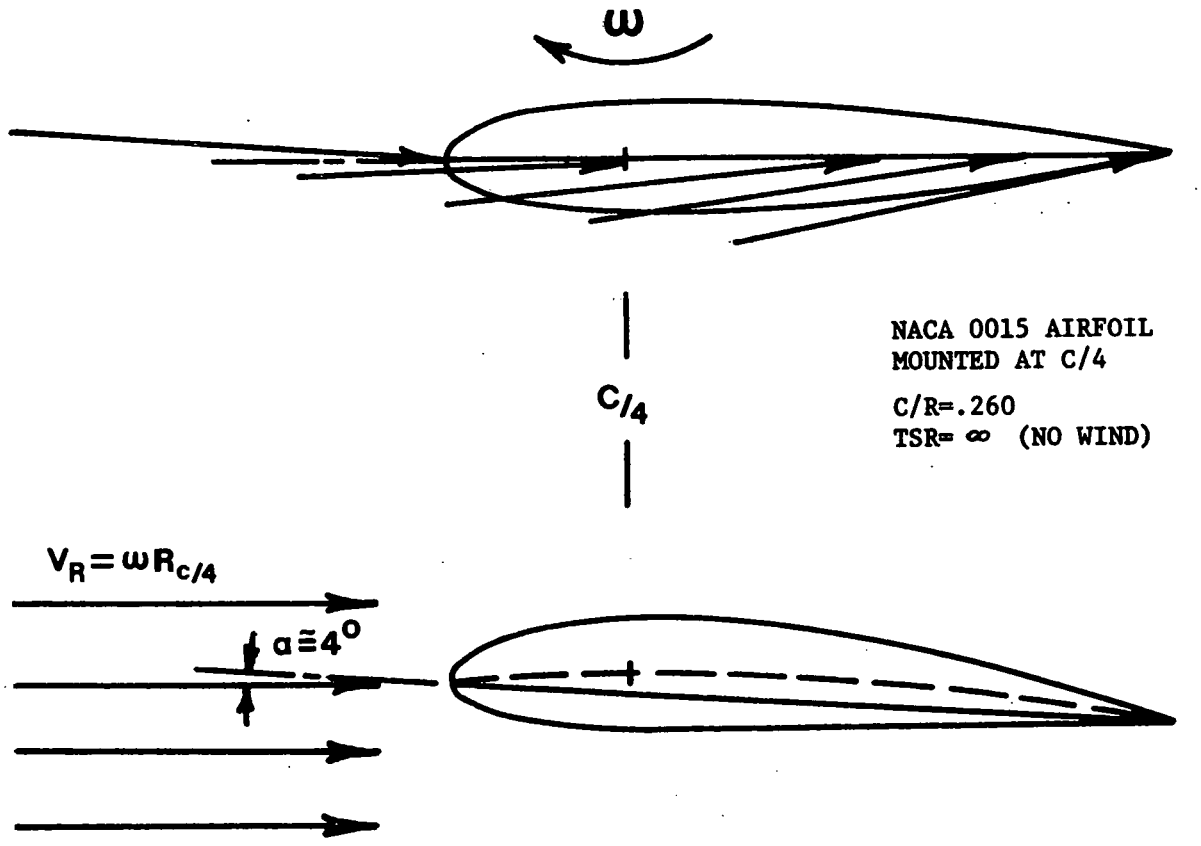

Figure 10. Geometric airfoils in curved flow transform to equivalent virtual airfoils in rectilinear flow.

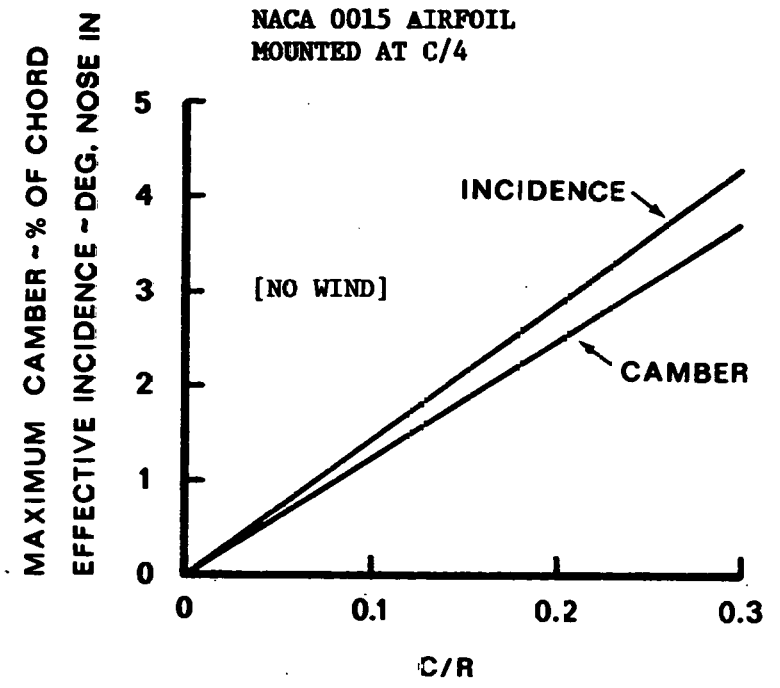

Figure 11. Camber and incidence resulting from flow curvature vary linearly with C/R.

variation in Re results. Strictly speaking, this Re variation is not a flow curvature effect. But its influence is inextricably linked to the unique aerodynamics of Darrieus turbines. Therefore, the Re variation phenomenon will be briefly treated here in order to present a qualitative view of its significance.

Reynolds number is given by

$$Re = V\ell/\nu \quad , \tag{22}$$

where V is the fluid velocity, ℓ is the body characteristic length (the blade chord C), and ν is the kinematic viscosity. For simplicity, V is normally taken to be the blade rectilinear velocity at the distance R, so that a nominal Re can be defined as

$$Re = \omega RC/\nu \quad . \tag{23}$$

Then the aerodynamic coefficients assumed for blade analysis are those for the chosen airfoil shape at the Re calculated from Equation 23.

In fact, V depends upon θ and is given by

$$V_R = \omega R(1 + \varepsilon^2 - 2\varepsilon \sin\theta)^{\frac{1}{2}} \quad , \tag{24}$$

where ε is the inverse tip speed ratio. Then the instantaneous Re is

$$Re' = \frac{\omega RC}{\nu} (1 + \varepsilon^2 - 2\varepsilon \sin\theta)^{\frac{1}{2}} \quad . \tag{25}$$

The angle of attack defined at the blade mounting point is

$$\alpha = \alpha_B + \theta - \arctan\left(\frac{\sin\theta - \varepsilon}{\cos\theta}\right) - \pi/2 \quad , \tag{26}$$

and for 90° blade pitch, $\alpha_B = \pi/2$, and

$$\alpha = \theta - \arctan\left(\frac{\sin\theta - \varepsilon}{\cos\theta}\right) \quad . \tag{27}$$

From Equations 25 and 27 it can be seen that both Re and α depend on blade location and tip speed ratio. For illustrative purposes it is convenient to define a relative Reynolds number as the ratio of the instantaneous Re' to the nominal Re and plot this paramater versus α. The result is shown in Figure 12 for a range of TSR.

It is apparent from Figure 12 that the orbiting blades experience a large fluctuation in Reynolds number relative to the nominal value. Assumption of the nominal value as the basis for aerodynamic coefficients is a tenuous proposition at best. What time lag may exist between the achievement of a given Re and the exhibition of aerodynamic properties associated with steady flow at that Re is unknown. Perhaps the best way to treat this Re variation is to simply consider it as part of the aggregate effects of flow unsteadiness. In any case it is certainly further evidence of the aerodynamic complexity of Darrieus turbines.

3.6 Summary

Test data for the WVU outdoor turbine suggested that blade aerodynamics were atypical of the symmetrical airfoils used and

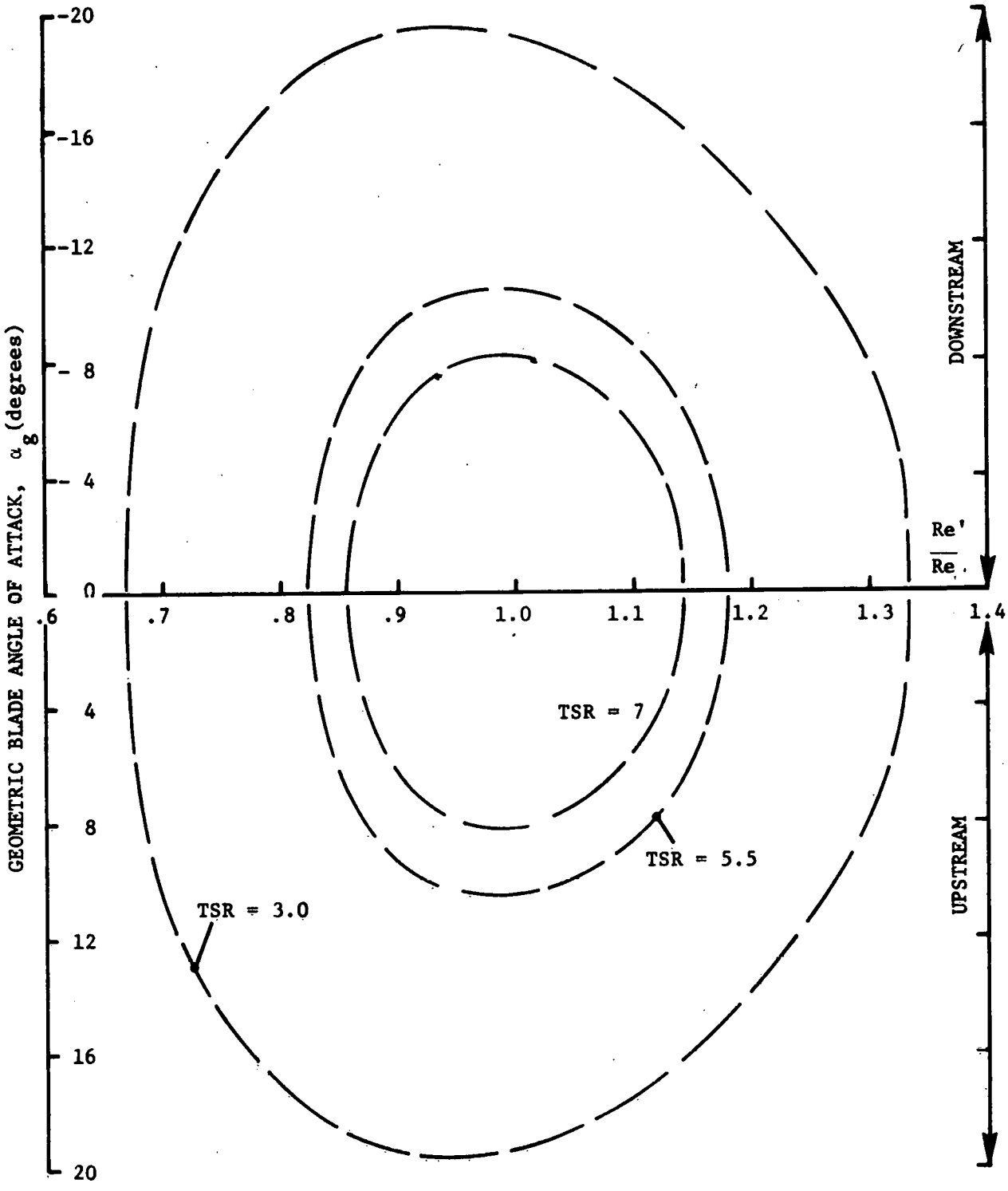

Figure 12. Illustration of the Reynolds number variation with angle of attack(and orbital position)

that serious performance degradation resulted for large C/R. Analysis of the idiosyncrasies of curved flow revealed several possible explanations. First, the radial pressure gradient in the blade boundary layer is an order of magnitude greater than normal for curved flows. It is suspected that this will result in premature flow separation over at least part of the blade orbit with attendant loss of lift and increased drag. Second, the orbital blade motion produces circular streamlines from the blade point of reference. Thus, the local velocity and angle of attack change at every chordwise location on the blade, as is the situation for cambered airfoils. Conformal mapping transforms the geometric airfoil to some equivalent virtual airfoil having additional camber and incidence. Turbine performance follows the aerodynamics of the virtual airfoil and will differ markedly from that expected on the basis of the aerodynamics of the geometric airfoil. Finally, owing to the cyclic variation of relative inflow velocity, Reynolds number varies with blade orbital position. At moderate TSR these Re excursions can be quite large. For turbines operating at low Re (say Re below 600,000) both lift and drag will be sensitive to θ. It is uncertain what effect this will have on net turbine performance.

Apparently, flow curvature effects are significant determinants of Darrieus turbine aerodynamics and performance. Of the three phenomena noted, virtual camber seems to be the most important.

Fortunately, its analysis can proceed with the aid of simple experimental tests and published sectional airfoil data. The investigation of centrifugal effects and Re variation must be deferred.

4. The Effects of Virtual Camber on Airfoil Aerodynamics

4.1 Drag from Turbine Tests Compared to Sectional Airfoil Data

The experimental drag curves of Figures 13, 14 and 15 were derived from test data as outlined in Section 2 and detailed in Reference 3. NACA 0015 airfoil sectional data [11] used for comparison were corrected for finite span effects. For the small blades, Figure 13, the drag at positive α compares well except at the large α corresponding to high lift coefficients. This could only be explained by the loss of planform efficiency in the noted range. This may result from premature flow separation associated with centrifugal effects. For the large blades, Figure 14, the experimental drag agrees poorly with the sectional data. $C_{D_{min}}$ is approximately 75% greater than expected and it occurs at a large negative α (about -5°). Recall that the conformal transformation procedure predicts an induced angle of incidence of 3.7° which would in large part account for the α shift. As with the small blades, a much reduced planform efficiency is indicated for the large blades. Figure 15 compares the small and large blades and clearly illustrates the disparate drag characteristics.

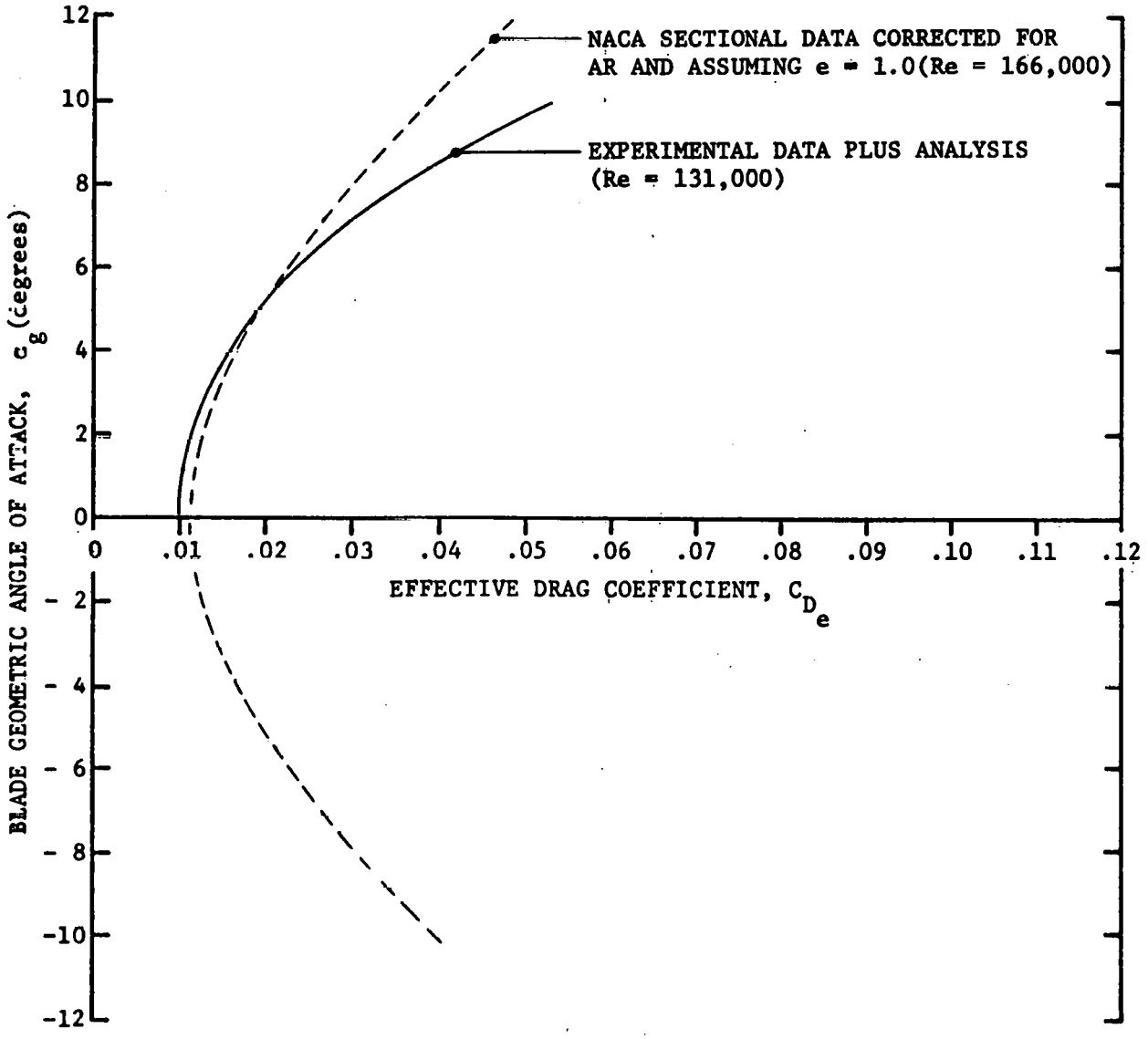

Figure 13. Comparison of experimentally determined drag polar(C_{D_e} vs α_g) for small blades(C/R = .114, AR = 18.7) to NACA sectional data

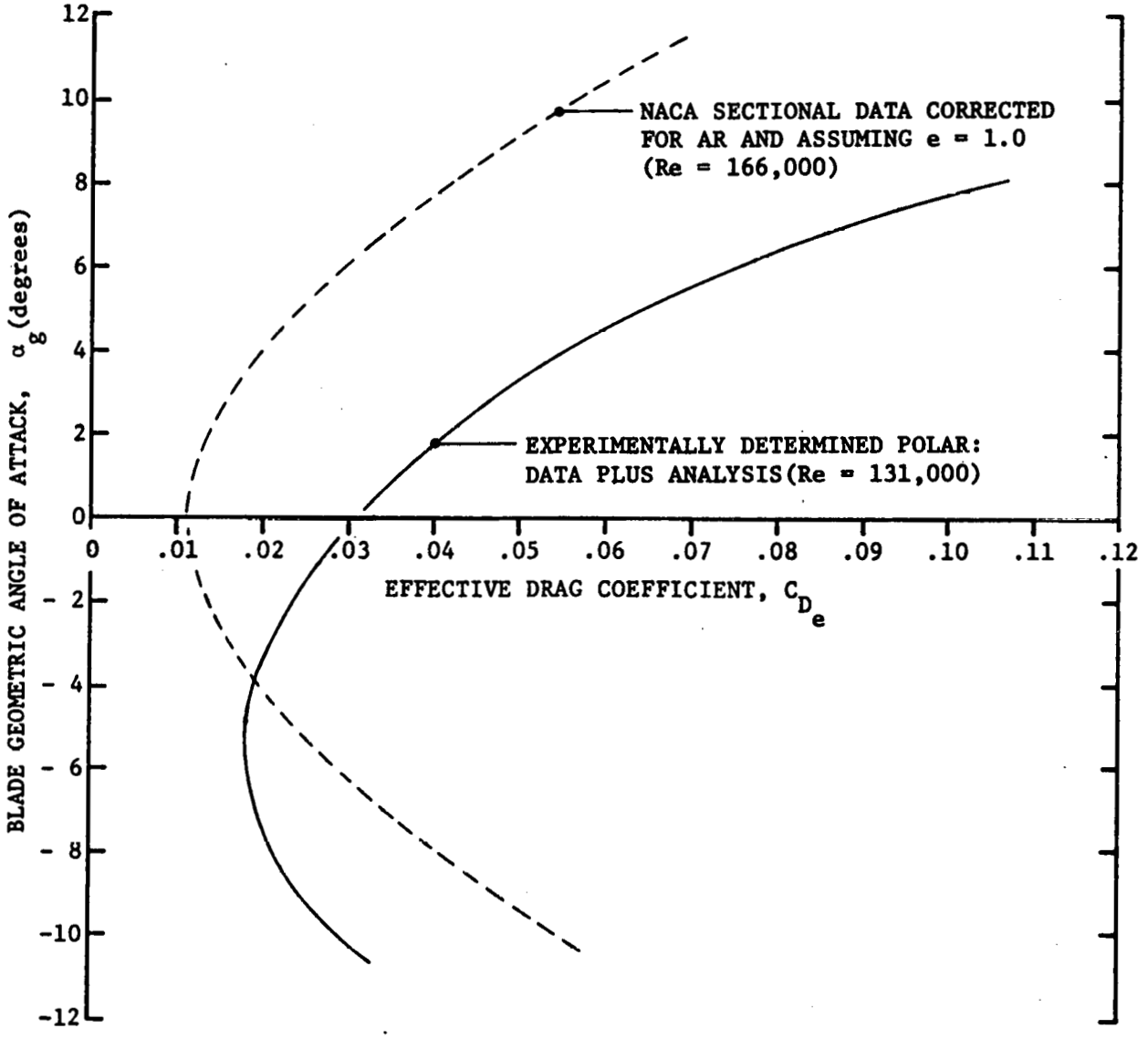

Figure 14. Comparison of experimentally determined drag polar (C_{D_e} vs α_g) for large blades (C/R = .260, AR = 8.2) to NACA sectional data

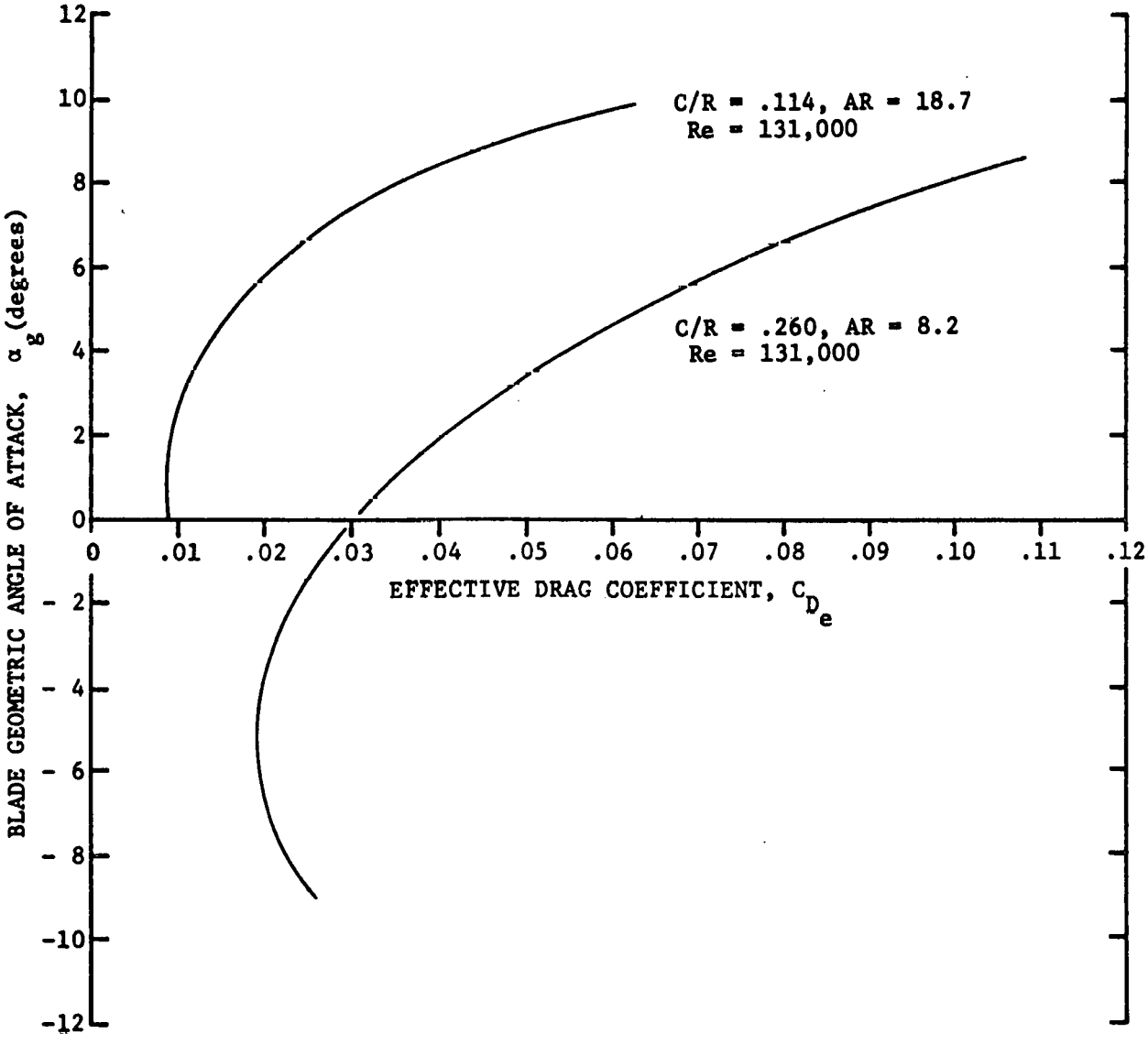

Figure 15. Drag polars(C_{D_e} vs α_g) from experimental data

It was thought that this drag discrepancy might result from airfoil shape or surface roughness differences. Sections of each blade were tested in the WVU low speed wind tunnel [5]. The results in Figure 16 show only minor differences in drag coefficients when the airfoils are in rectilinear flow (the wind tunnel), but the experimentally verified large differences in drag coefficients obtained in the outdoor turbine tests are undeniable. It is unlikely that the aforementioned Reynolds number variation is responsible, since both large and small blades experience the same relative cyclic changes. Note also in Figure 16 that $C_{D_{min}}$ for the turbine blades does not decrease with increasing Re as is well documented in the literature and demonstrated by the wind tunnel data. One must conclude then that these unusual drag characteristics result from the flow curvature, centrifugal, and virtual camber effects.

4.2 Lift-Drag Relationships for the Virtual Airfoils

The WVU turbine was instrumented to provide torque data from which the effective drag could be deduced. Though it was not possible to determine the lift characteristics directly, an approximation to the C_L-C_D relationship was obtained by analysis. This information is useful in comparing the aerodynamics of the virtual and geometric airfoils.

On the basis of published data [11, 12] and numerical vortex model studies [13], a sectional lift curve slope of 0.10 per degree is assumed for the NACA 0015 airfoil in the linear range. Also the virtual camber and incidence predicted by the conformal analysis is assumed to

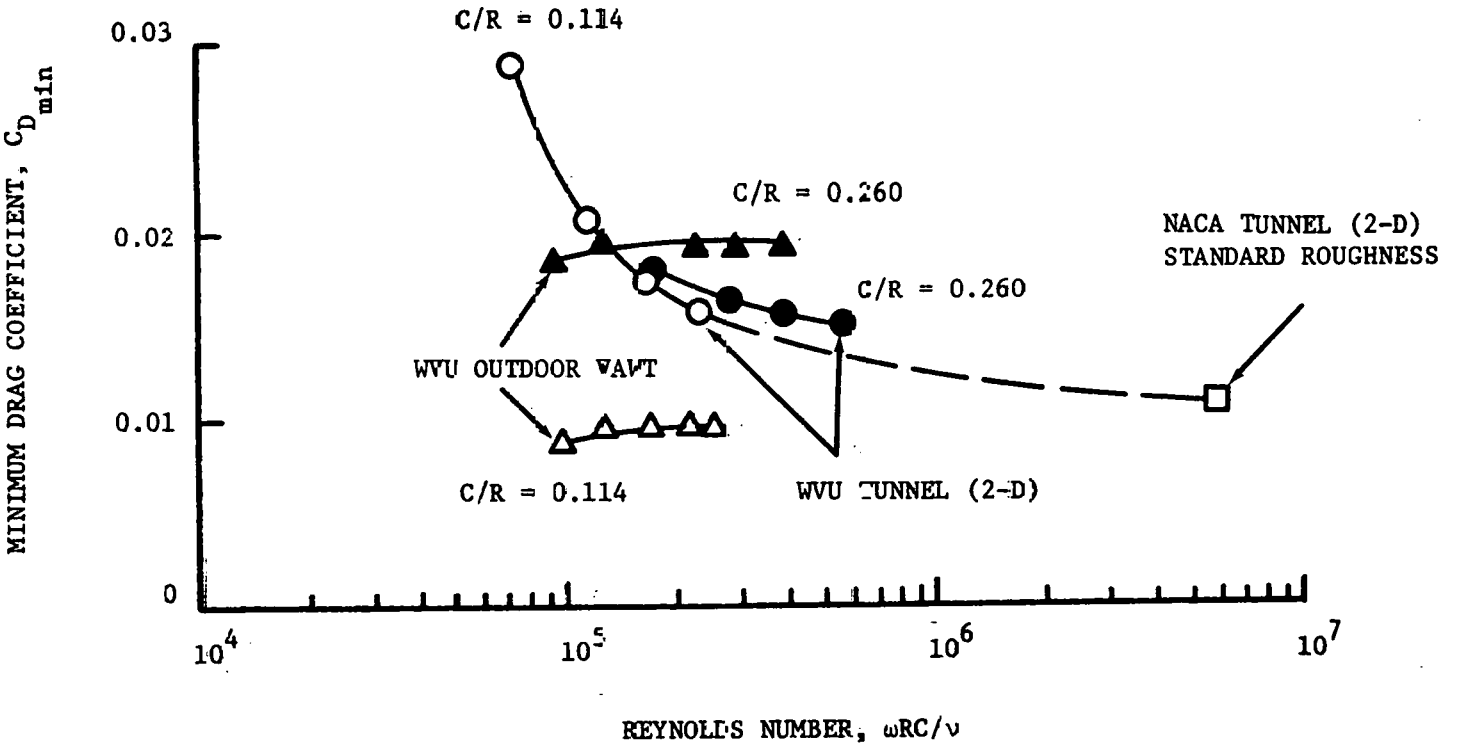

Figure 16. Comparison of minimum drag coefficient from wind tunnel and outdoor turbine tests

be correct. The effective angle of incidence which results from flow curvature is defined by the symbol α_i. The geometric angle of attack at the reference point on the blade chord is given the symbol α_g. The combination of the two is the virtual angle of attack α_v, which is defined as the angle between the relative inflow velocity and the chord at the reference point. Therefore,

$$\alpha_v = \alpha_g + \alpha_i \quad . \tag{28}$$

For airfoils in rectilinear flow, $\alpha_v = \alpha_g$.

Examination of section lift data shows an upward shift in C_L at $\alpha_v = 0°$ of 0.10 for every 1% of camber. Thus, the small blades with virtual camber of 1.4% have $C_L = 0.14$ at $\alpha_v = 0°$, and the large blades with virtual camber of 3.2% have $C_L = 0.32$ at $\alpha_v = 0°$. Virtual incidence causes a shift in the angle of attack axis of 1.6° for the small blades and 3.7° for the large blades. These characteristics are reflected in the $C_L - \alpha$ curves of Figure 17. It is of immediate interest to note the error resulting from neglecting virtual incidence and camber. For example, at $\alpha_g = 0°$ one would expect $C_L = 0$, where actually $C_L = 0.30$ for the small blades and $C_L = 0.69$ for the large blades

From the test data α versus C_D is known, and from Figure 17 C_L versus α is obtained. The combination gives the C_L-C_D polars of Figures 18 and 19. These are compared to sectional data

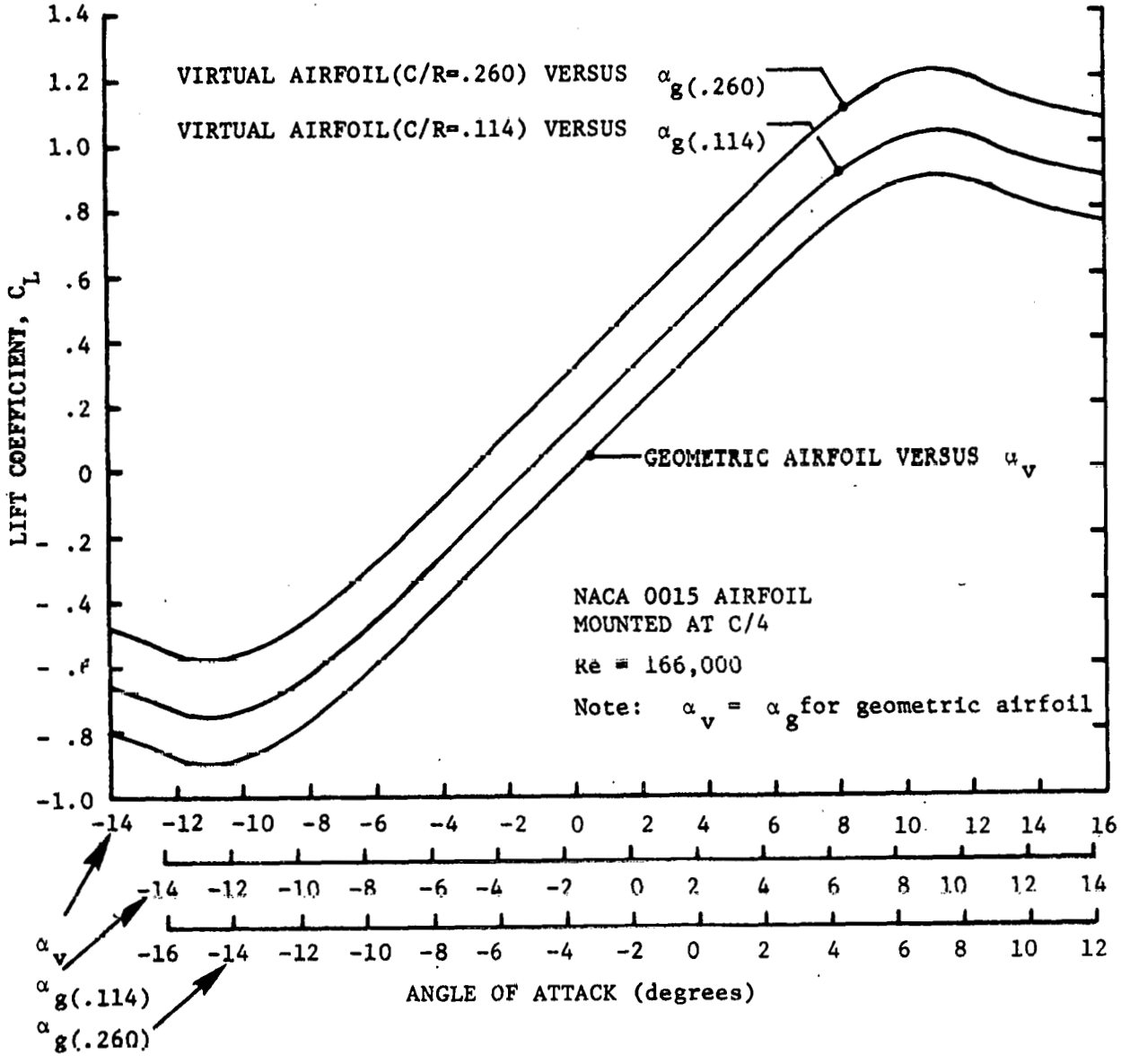

Figure 17. Sectional lift curves for virtual and geometric airfoils

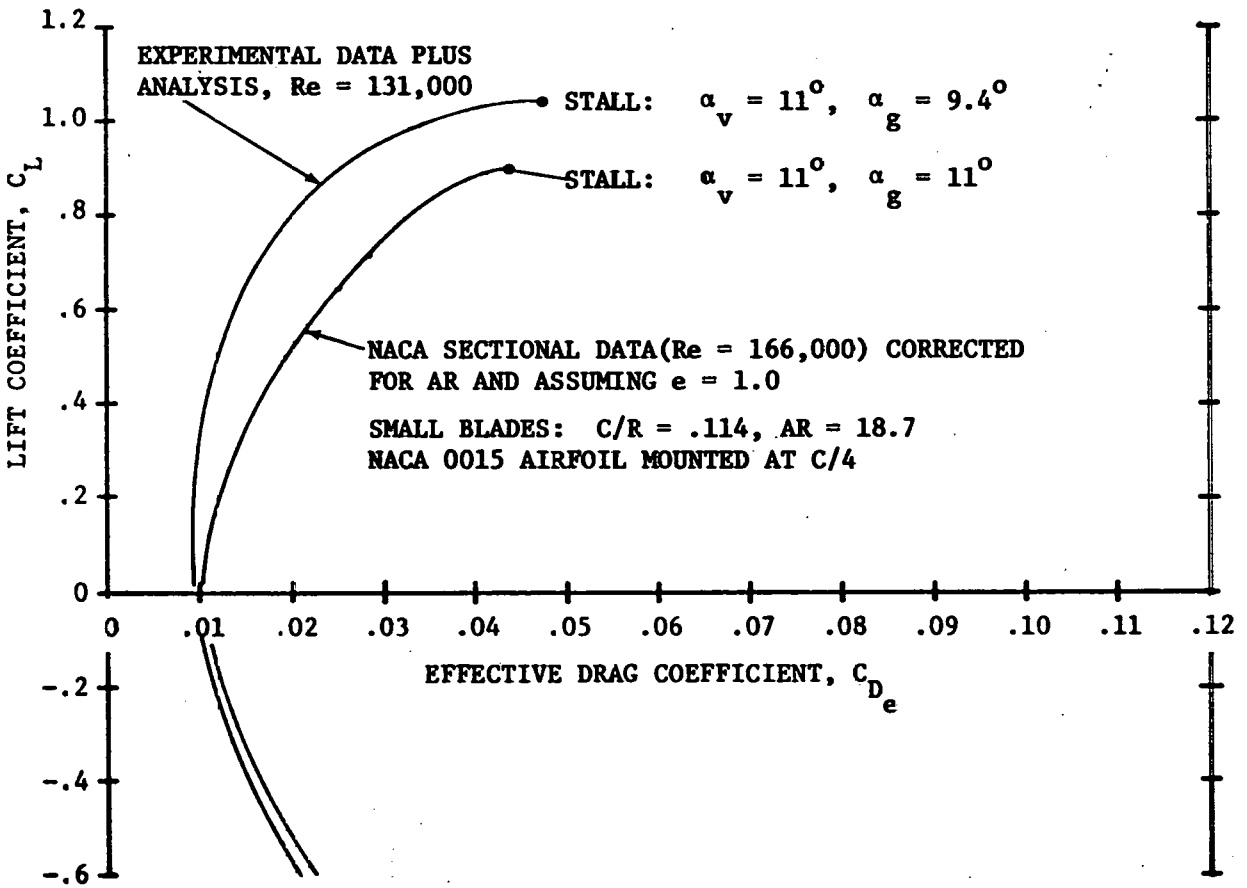

Figure 18. Comparison of drag polar from experimental data plus analysis to NACA sectional data

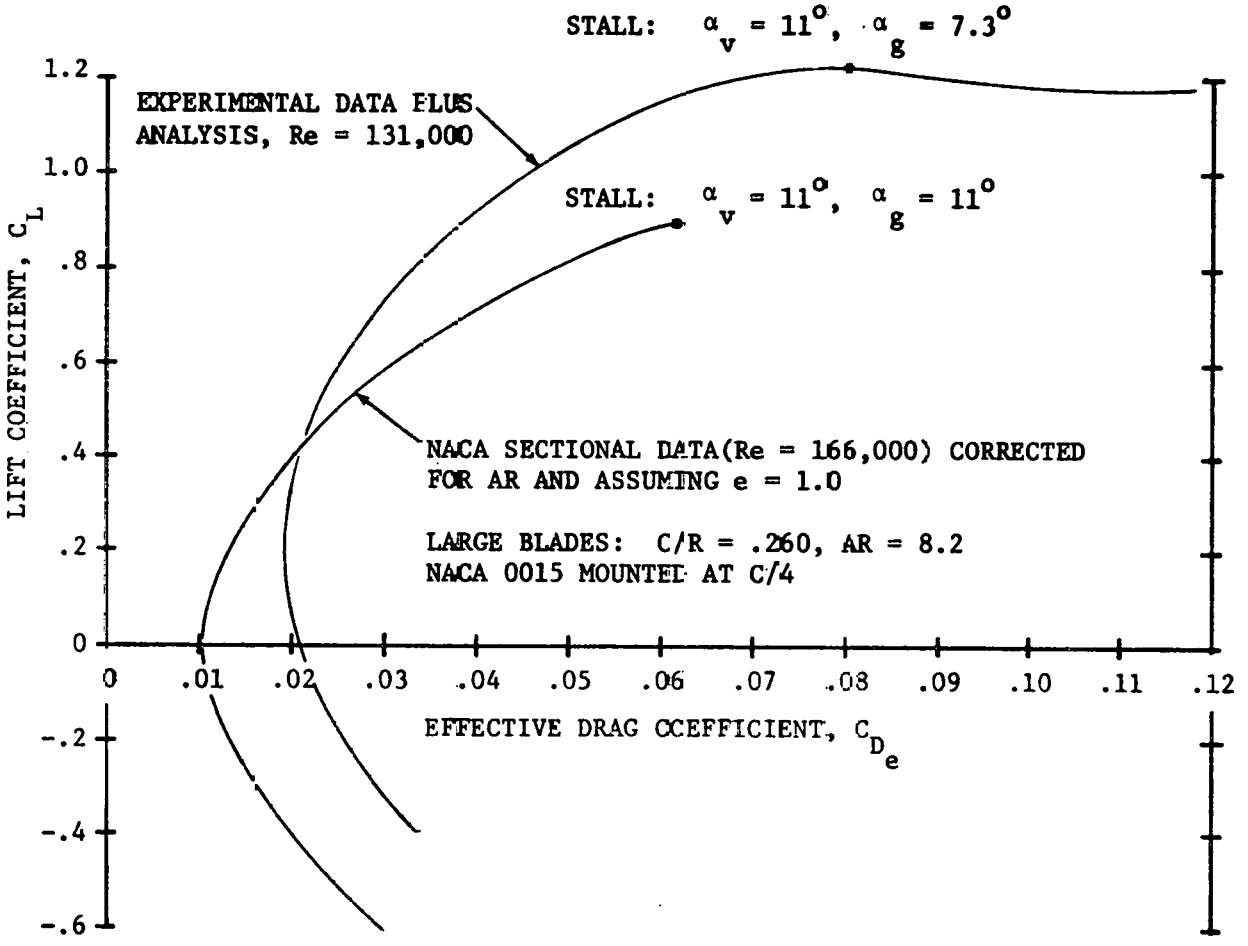

Figure 19. Comparison of drag polar from experimental data plus analysis to NACA sectional data

corrected for finite span effects and assuming a planform efficiency of 100%. The sectional data give a polar shape typical of symmetrical airfoils, that is, $C_{D_{min}}$ occurs at $C_L = 0$. However, the virtual airfoils have $C_{D_{min}}$ at some non zero lift and this shape typifies cambered airfoils. The influence of the curvature index on virtual aerodynamics is demonstrated by comparing C_L-C_D for the large and small blades as shown in Figure 20. Recall that the two blades exhibited essentially the same drag coefficients in wind tunnel tests, but note the discrepancy in C_L-C_D curves when mounted on the turbine.

The preceeding discussion illustrates the effects of flow curvature on the lift and drag of airfoils. However, examination of the C_L-α or C_L-C_D curves by themselves does not demonstrate the impact of flow curvature on turbine performance, since the two act in combination to produce torque. The following section considers the mechanism of torque production and the manner in which it is affected by virtual aerodynamics.

4.3 Influence of Virtual Aerodynamics on Turbine Torque

Besides the boundary layer centrifugal effects, flow curvature introduces virtual camber and incidence. Virtual camber influences airfoil aerodynamics in two important ways: first, it causes an upward shift in the lift curve, and second, it introduces a moment coefficient which produces counter torque over the entire blade orbit. Virtual incidence acts to shift the lift curve to the left

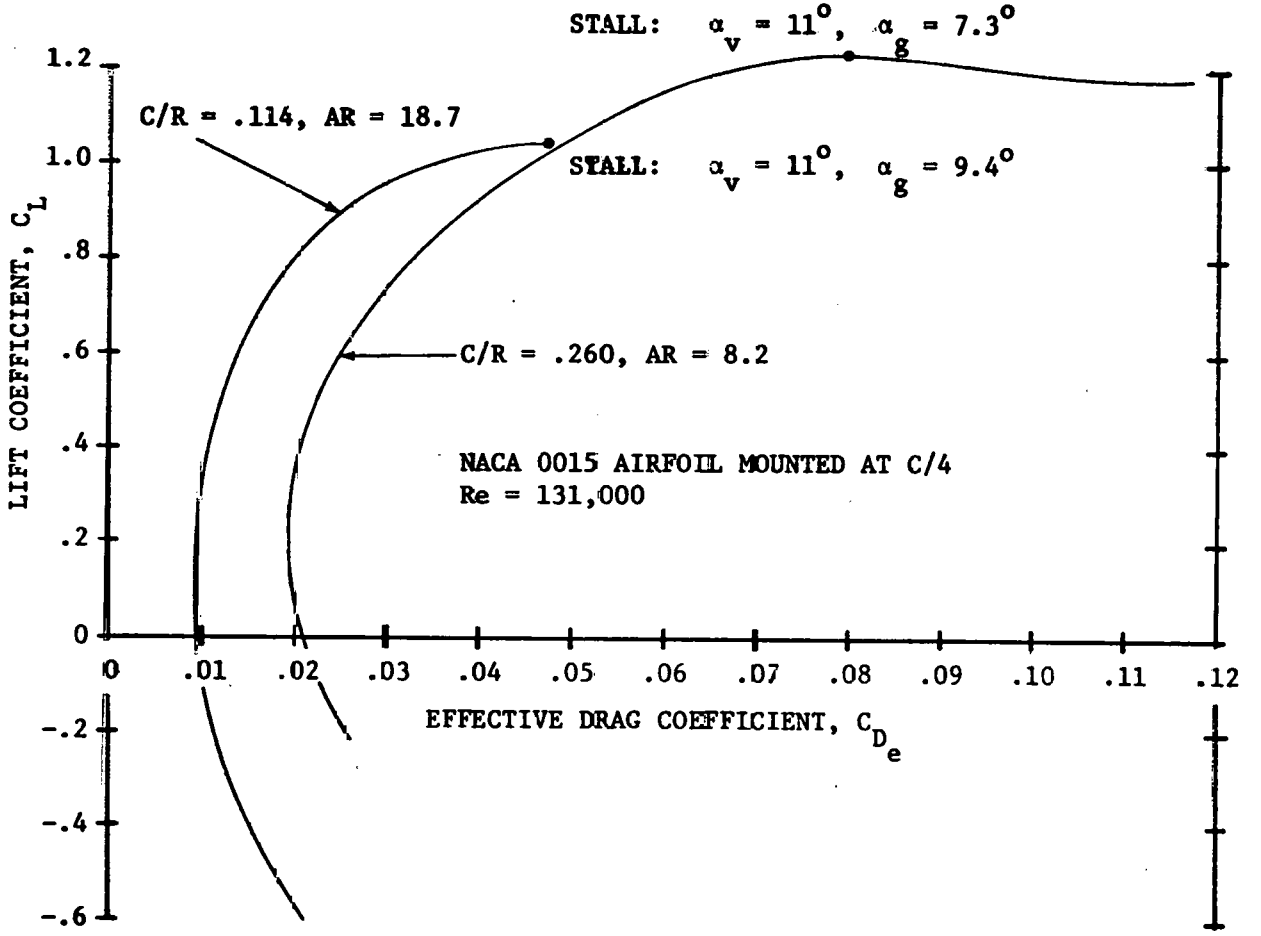

Figure 20. Drag polars from experimental data plus analysis: comparison of large and small blades

on the α- axis of the C_L-α curve. The manner in which these properties alter torque production can be observed with the aid of the equation for instantaneous torque. Recalling that the countertorque produced by the drag and moment can be characterized by an effective drag coefficient, C_{D_e}, the expression for the instantaneous blade torque is

$$T_B(\theta) = \tfrac{1}{2}\rho V_R^2 \, CbR \, [C_L \sin(\theta-\beta) - C_{D_e} \cos(\theta-\beta)] \quad . \qquad (29)$$

From the lift-drag-angle of attack relationships, Equation 24 for V_R, and Equation 27 for α, $T_B(\theta)$ can be calculated as a function of orbital position, θ. A plot of $T_B(\theta)$ versus θ will illustrate the manner of power extraction since C_p is proportional to $T_B(\theta)$. A more convenient parameter is obtained by noting that the instantaneous power coefficient for the blade is

$$C_p(\theta) = \frac{T_B(\theta)\omega}{\rho V_\infty^3 \, bR} \qquad (30)$$

Using Equation 29 for $T_B(\theta)$, Equation 24 for V_R, and noting that TSR = $\omega R/V_\infty$, Equation 30 becomes

$$C_p(\theta) = (TSR)^3 \left(\frac{C}{2R}\right)(1+\varepsilon^2-2\varepsilon\sin\theta)[C_L \sin(\theta-\beta) - C_{D_e} \cos(\theta-\beta)]. \quad (31)$$

Since comparisons of airfoils must be made at particular values of TSR and C/R, terms containing only these parameters may be moved to the left hand side of Equation 31. An instantaneous measure of merit for the airfoil is thus defined as

$$\mu(\theta) = \frac{C_p(\theta)}{(TSR)^3\left(\frac{C}{2R}\right)} = (1+\varepsilon^2-2\varepsilon\sin\theta)[C_L \sin(\theta-\beta) - C_{D_e} \cos(\theta-\beta)] \quad (32)$$

Note that the term $(1 + \varepsilon^2 - 2\varepsilon\sin\theta)$ is simply the square of the relative inflow velocity at θ nondimensionalized by the nominal blade rectilinear velocity, ωR. That is,

$$(1 + \varepsilon^2 - 2\varepsilon\sin\theta) = \left(\frac{V_R}{\omega R}\right)^2 \quad . \tag{33}$$

Integrating $p(\theta)$ over the entire orbit gives a net airfoil measure of merit defined by

$$P = \int_0^{360} p(\theta)d\theta \quad . \tag{34}$$

The significance of this parameter is shown by the following illustration.

Consider the large blades of C/R = .260 in fixed pitch operation at $\alpha_B = 90°$ and TSR = 5.5, and assume the blade mounting point is the quarter chord. Using the conformal transformation procedures outlined in Section 2.4 the virtual camber and incidence are determined as functions of orbital position, θ. These are shown in Figure 21. Although y_c/C and α_i vary with θ, it can be shown that their mean value is that determined by the conformal transformation at TSR = ∞ and $\theta = 0°$. Therefore, in order to simplify the analysis, these mean values will be assumed constant over the entire orbit. As noted previously, for the large blades, y_c/C is 0.032 (3.2%) and α_i is 3.7°. Thus, the virtual aerodynamics of the large blades may be obtained by applying the proper aspect ratio corrections to the $C_L - \alpha$ curve of Figure 17, and from the C_L-C_D curve of Figure 19.

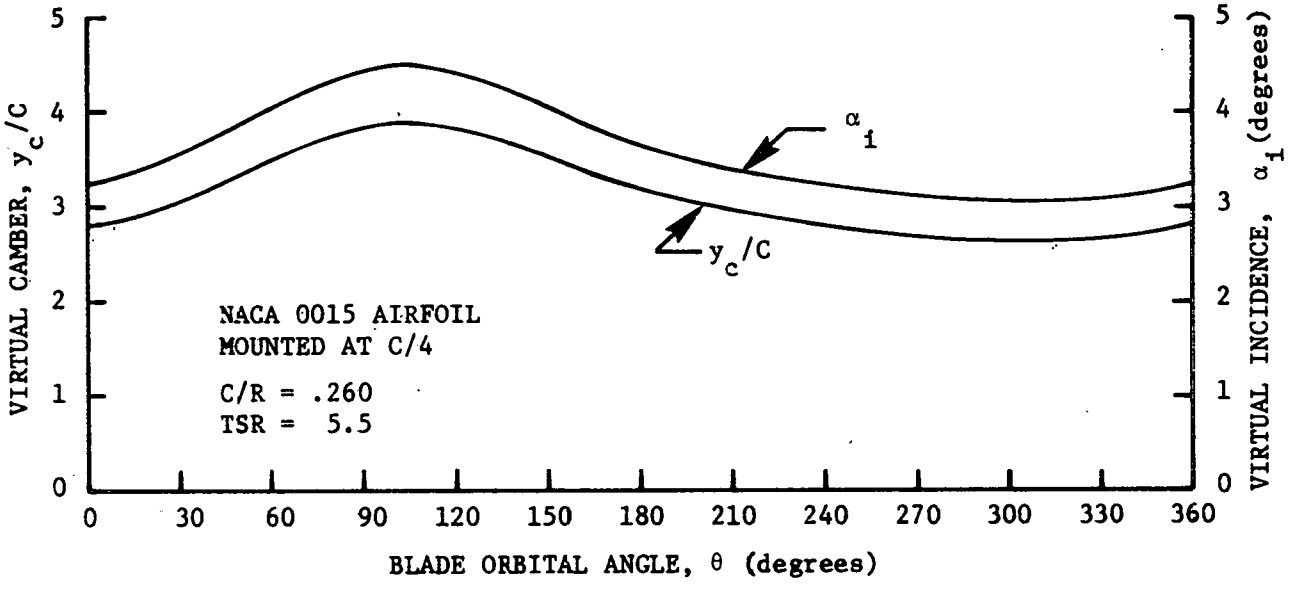

Figure 21. Example of the variation of virtual camber and incidence with blade orbital position

Applying the conformal transformation procedures to the problem, with geometry as defined above, gives the α_v versus θ plot* of Figure 22. This figure provides considerable insight regarding torque production and power extraction. Consider specifically the regions labelled (1) in Figure 22. Neglecting virtual incidence, the maximum angle of attack reached at TSR = 5.5 is assumed to be $\alpha_g = 10.5°$. But virtual incidence causes an increase in this value to $\alpha_v = 13.8°$ and the stall angle is exceeded. Associated with blade stall are large drag increases which diminish torque production. Thus in regions (1), even though virtual camber might result in higher than expected lift coefficients, it is probable that reduced torque and a lower C_p will result. Regions (1) are therefore areas of diminished efficiency compared to the properties expected of the geometric airfoil. Consider next the areas labelled (2). It can be shown that positive torque results from a combination of positive C_L and positive α on the upstream side of the turbine ($90°>\theta>270°$), or from the combination of negative C_L and negative α on the downstream side of the turbine ($90°<\theta<270°$). These conditions are violated in regions (2). For example, between 90° and 110°, α_v and C_L are positive and between 110° and 129° even though α_v is now negative C_L is still positive. Even though little power is normally extracted in these θ regions (owing to low C_L at low α), virtual aerodynamics make the situation much worse since countertorque results. Regions (2), therefore, also diminish turbine

---

*Consistent with the assumption of the constant mean α_i value, rigid adherence to the α_v schedule of Figure 22 was not maintained. Rather it was assumed that the relationship $\alpha_v=\alpha_g+\alpha_i$ was sufficiently accurate.

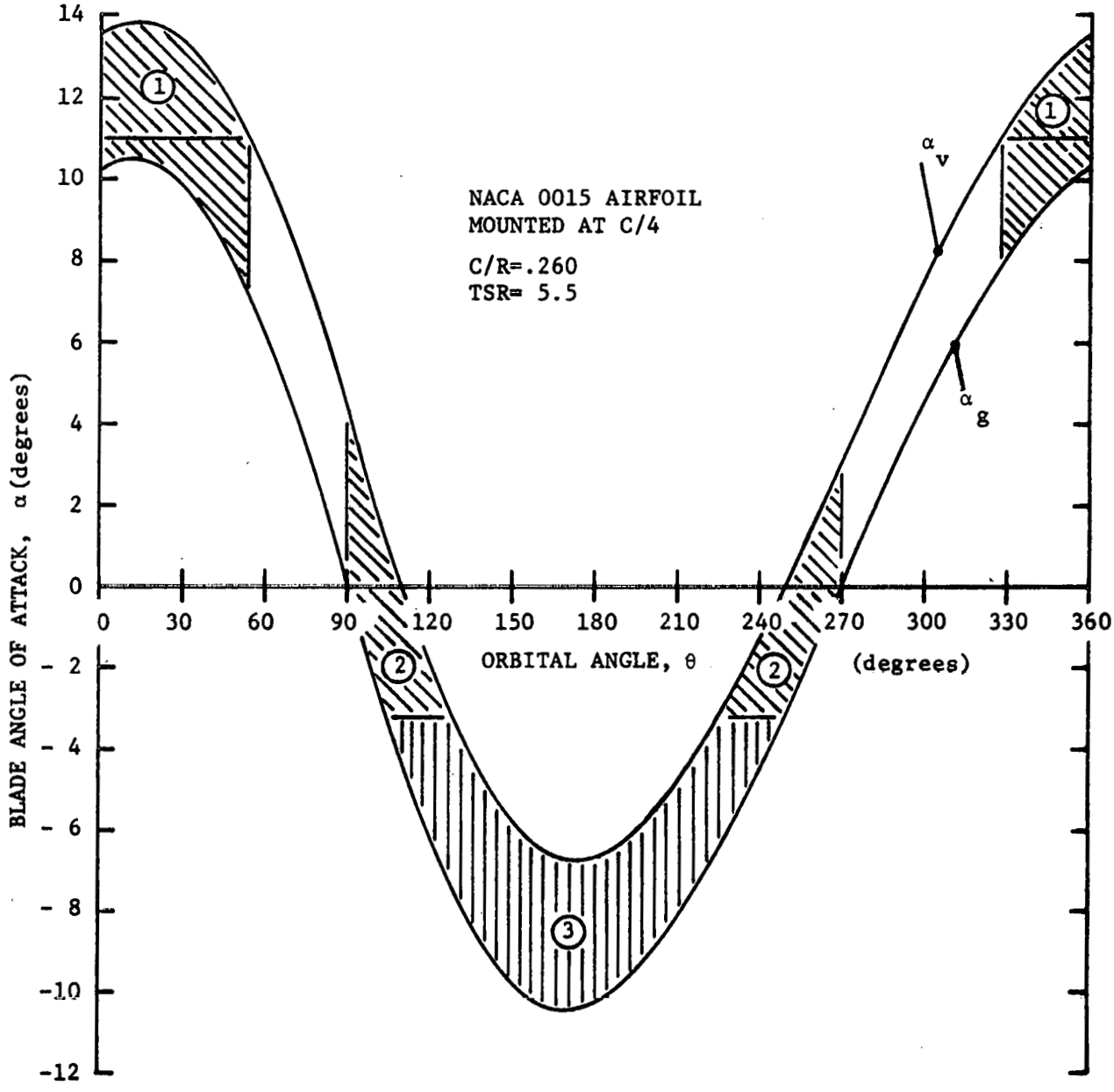

Figure 22. Comparison of virtual and geometric angles of attack

efficiency. Region (3) is similarly an area of diminished efficiency, since α_v is much less than α_g here, and also because the virtually cambered airfoils have very low C_L at negative angles of attack.

From the preceeding analysis it can be seen that if one does not properly compensate for virtual aerodynamics, significant performance degradation may occur. This conclusion is supported by the results of Figure 23 where $p(\theta)$ is plotted for the virtual airfoil and compared to $p(\theta)$ for the geometric airfoil. The areas of diminished power follow closely those predicted from analysis of Figure 22. Note the sharp drop in $p(\theta)$ at approximately 50° and 330° where blade stall occurs. And on the downstream side of the turbine $p(\theta)$ is everywhere reduced since the virtual airfoil produces very little lift at negative angles of attack. Integrating the curves of Figure 23 shows that the airfoil measure of merit P for the virtual airfoil is only 15% of that expected of the geometric airfoil. This result would of course change at different TSR and C/R. In fact analysis of the $p(\theta)$ plot of Figure 24 for the small blades reveals that P is decreased by only 8%. It is interesting to note that for the small blades efficiency actually increases on the upstream side of the turbine as indicated by the greater area under the curve. The efficiency loss on the downstream side more than offsets the front side gain, however. The situation suggests that some combination of virtual camber and incidence may in fact produce a net gain.

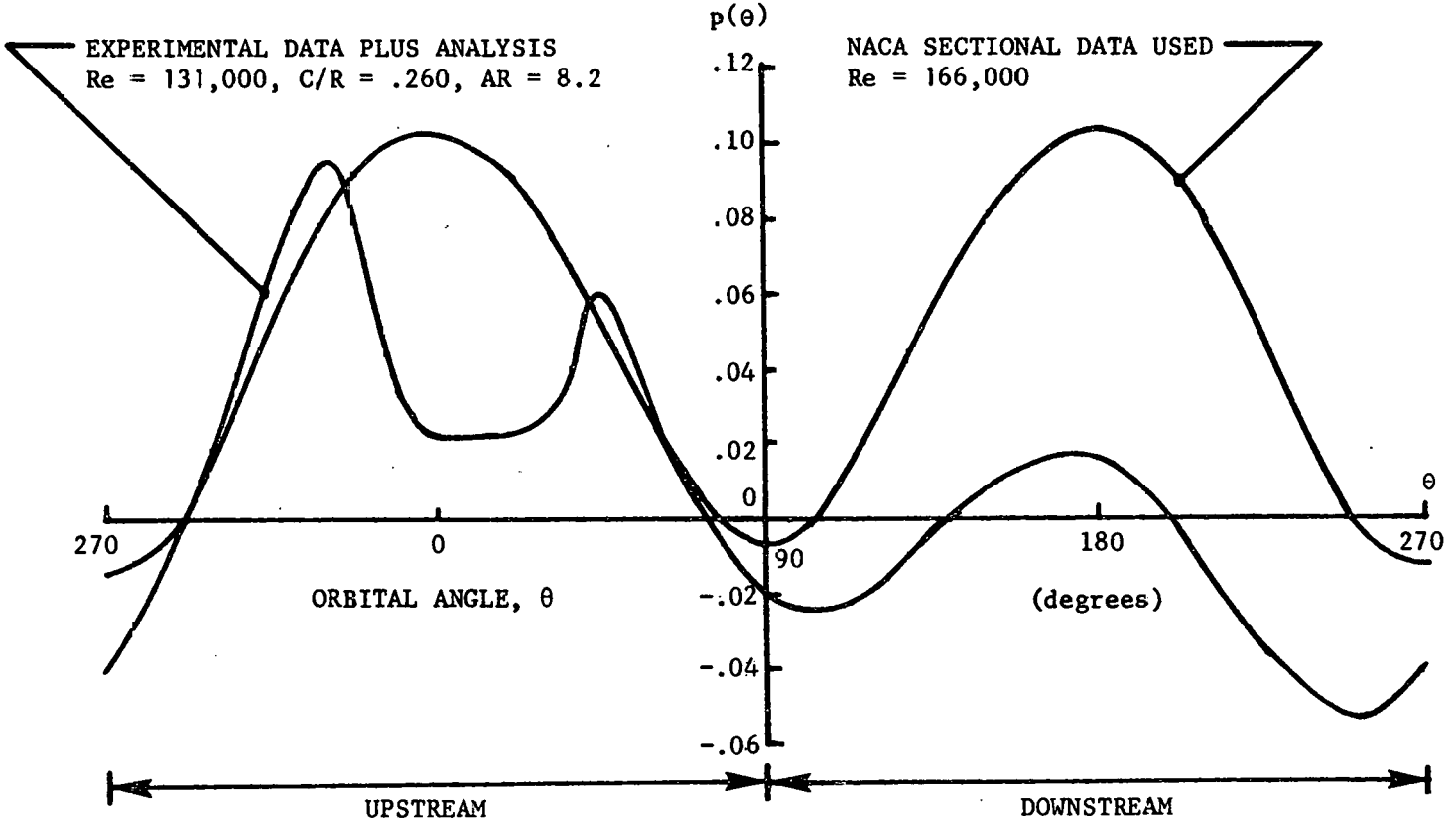

Figure 23. The instantaneous measure of merit $p(\theta)$ is proportional to torque output and C_p. Here the large blades are compared to expectations for the NACA 0015 airfoil.

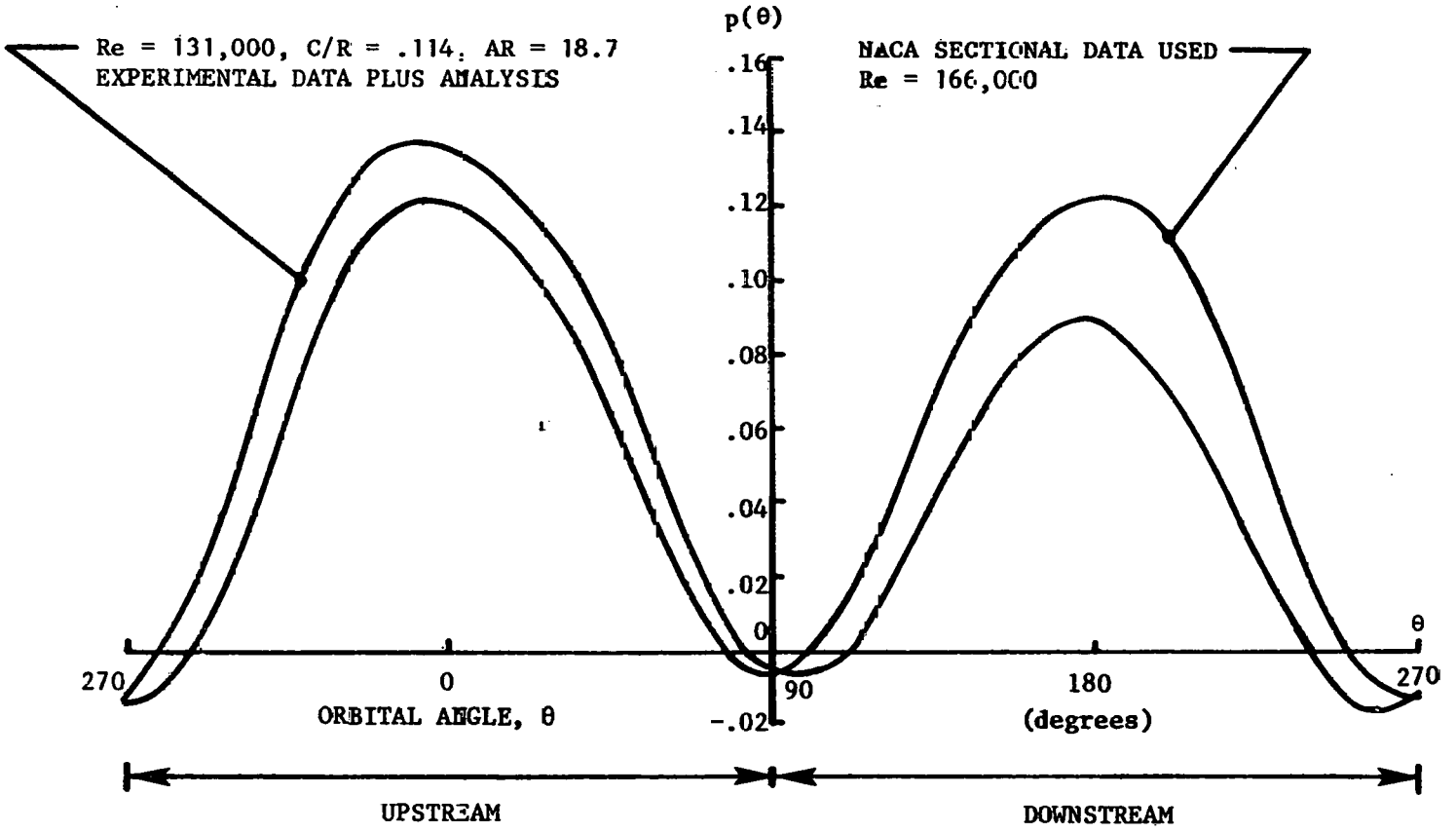

Figure 24. The instantaneous measure of merit p(θ) is proportional to torque output and C_p. Here the small blades are compared to expectations for the NACA 0015 airfoil.

Figure 25 is the $p(\theta)$ plot for both the large and small chord virtual airfoils. It is clear from this figure, that large C/R has a disasterous effect on power extraction.

No mention has been made in the previous discussion of the importance of flow blockage and unsteadiness. These phenomena are important and cannot be neglected in considering turbine performance. Both depend on rotor solidity and so a choice of C/R cannot be made solely on the basis of flow curvature considerations. However, the preceeding analysis, which is based on the properties of the virtual airfoils, should still be valid for evaluating competing airfoils and pitch schedules. That is to say, if one airfoil has improved aerodynamics compared to another, it should still show an advantage regardless of the specific influence of other flow phenomena (blockage, unsteadiness, Reynolds number variation, and to a large extent, centrifugal effects). The $p(\theta)$ method is therefore a means of evaluating airfoils and their performance relative to each other; it cannot be used to accurately predict C_p.

5. Influence of Flow Curvature on Turbine Design

5.1 Overview

The designer is faced with several choices (regarding the turbine rotor geometry) which will influence aerodynamic efficiency and performance. These choices include blade airfoil section, rotor geometry

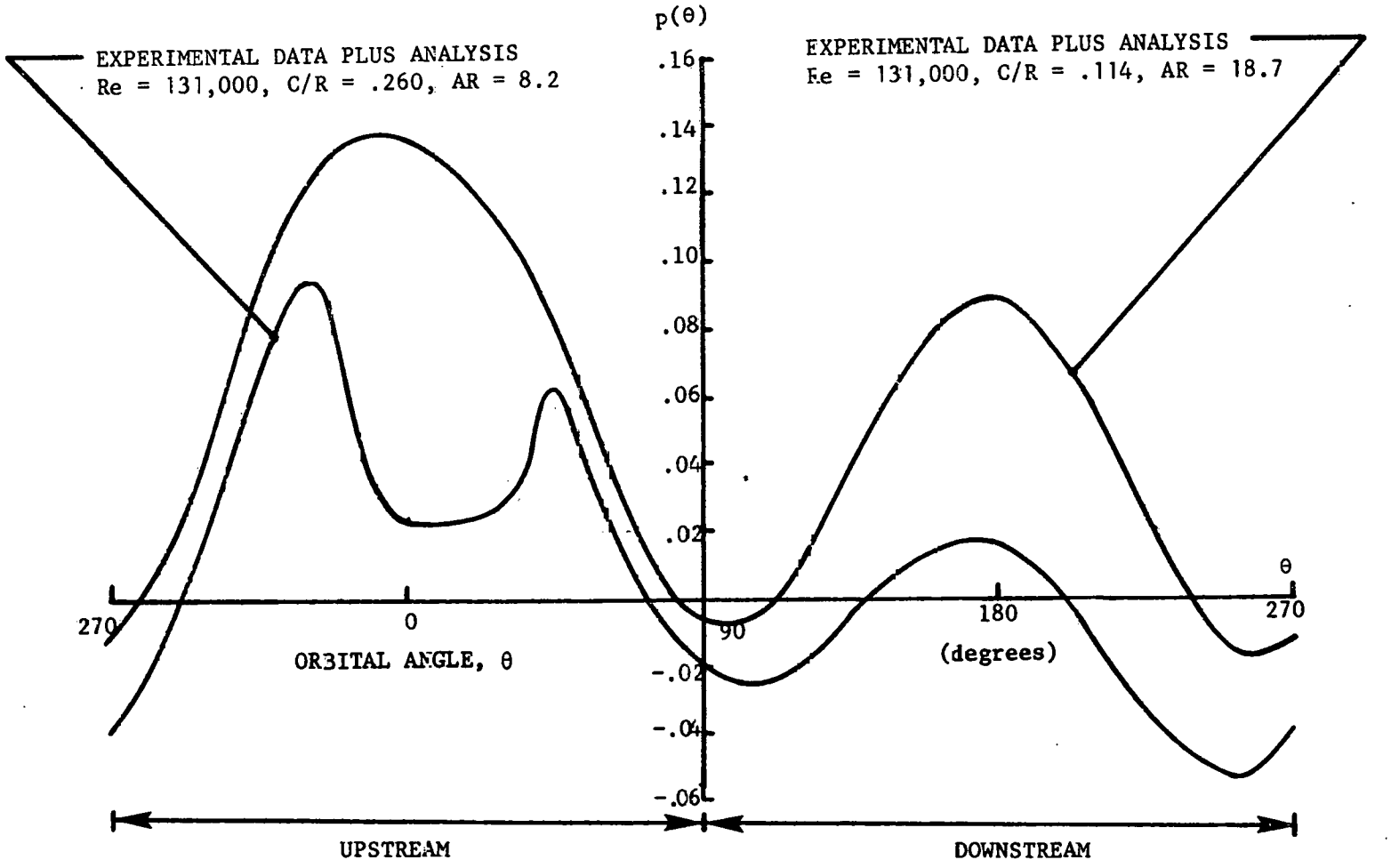

Figure 25. The instantaneous measure of merit $p(\theta)$ is proportional to torque output and C_p. Here the large and small blades are compared.

as defined by n_b, C/R, and b, and blade pitch schedule for variable pitch machines. Owing to its pronounced impact on blade aerodynamics, flow curvature must also be considered in turbine design.

Curvature index is the parameter which characterizes flow curvature. It defines the Froude number which characterizes centrifugal boundary layer effects, and also determines the virtual camber and incidence. Large C/R's produce significant detrimental aerodynamic changes and one might assume that they should be avoided. This is not necessarily true, since by understanding and using to advantage the mechanisms of virtual aerodynamics, large C/R blades remain viable choices. They may in fact be preferred because the desired rotor solidity can be achieved with fewer blades, obviously at lower cost. Furthermore, large blade chords imply high Reynolds numbers, and with them go improved lift and drag characteristics. So the choice of airfoil section, C/R, and blade pitch schedule can only be made intelligently upon proper consideration of flow curvature. The material which follows discusses several possibilities.

5.2 Fixed Pitch Turbines

Symmetrical airfoils have historically been chosen for Darrieus turbines because C_L-C_D characteristics are identical at positive and negative α corresponding to upstream and downstream orbital positions, and because C_M is zero and contributes no countertorque. However, virtual camber and incidence destroy the premise upon which the choice of symmetrical airfoils is based. For a given α_g more lift is

produced upstream than downstream, and the additional α_i may even cause blade stall at certain TSRs. The simplest way to alleviate this problem is to fabricate geometric airfoils whose virtual equivalents are the symmetrical airfoils originally chosen. The inverse conformal transformations of Appendix B would be used to design the geometric airfoil for the assumed TSR, C/R, and blade mounting point. Since this can be accomplished for any C/R, the objection to large C/R is obviated. The concept may be extended to the consideration of airfoils whose virtual equivalents really are cambered. These airfoils would experience increased power extraction on the upstream side of the turbine due to increased C_L, and the diminished efficiency on the downstream side might be more than offset by the upstream improvements. This seems particularly plausible since power extraction is asymmetric with respect to the cross wind axis as a result of flow blockage. At the present time it is not certain whether net power extraction will be increased by designing for front side or back side optimization. The option remains to explore this possibility by judicious choice of camber and initial blade pitch setting. Such a study can only be pursued experimentally or with the aid of an accurate model of the flow blockage.

5.3 Variable Pitch Turbines

The increased complexity of electro-mechanical pitch variation may be justifiable for large turbines, and the potential for advantageous use of virtual aerodynamics is enhanced for these machines. The interrelationship between virtual camber and incidence

has already been demonstrated. For a particular configuration the α_v versus θ relationship can be established as discussed in Section 4.3. It is then a simple matter to deduce the α_B versus θ schedule required to maintain the blade at its optimum pitch. The optimum is chosen so that $p(\theta)$ is maximized on the upstream and downstream sides of the turbine. This may require a rather large blade "flip" at $\theta = 90°$ and $\theta = 270°$ where α_g normally changes sign. Again power extraction will be asymmetric owing to both virtual camber and flow blockage. Note in Figure 17 that C_L, and therefore $p(\theta)$, is maximized at $\alpha_v = \pm 11°$, the blade stall angle. However, at this point on the upstream side $C_L = 1.22$ while downstream it is only -0.58. As is the case with fixed pitch operation it is not certain whether net power extraction will be increased by optimizing the front side or the back side. Of course, the option remains of returning to geometric airfoils whose virtual equivalents are symmetrical.

5.4 Variable Camber/Variable Pitch Turbines

As noted earlier, under certain conditions front side power extraction may be greatly improved as a result of virtual camber. This results from higher C_L at a given α_g and is demonstrated in Figure 24 for the small blades. Note also in Figure 23 for the large blades that had the blades not stalled at $\theta \simeq 50°$ and $\theta \simeq 330°$, $p(\theta)$ would have remained greater than expected over the entire upstream side. For variable pitch machines the stall problem can be avoided by adjusting the blade pitch schedule. However, the severe

power loss on the downstream side resulting from virtual camber and incidence must be considered. If the favorable effects noted on the front side could somehow be extended to the back side, overall efficiency would be greatly improved. This situation recommends serious consideration of electro-mechanically implemented variable camber.

Variable camber has been used extensively on fixed wing aircraft in the form of leading and/or trailing edge devices and all manner of boundary layer control devices. It is possible to apply these same principles to Darrieus turbine blades.* Cyclic manipulation of plain or split flaps should be no more difficult than cyclic manipulation of blade pitch. Combined with judiciously chosen virtual camber and control of blade pitch, power extraction enhancement should be substantial. It is of course questionable whether the greatly increased aerodynamic drag and moments of flapped airfoils could be overcome by the increased lift to yield a net improvement. However, the potential can be demonstrated simply by considering $p(\theta)$ at the optimum operating point of the blades. Figure 26 illustrates the situation by comparing the drag polars of a symmetrical NACA 0012 and a cambered NACA 4412 airfoil. In this example, a lift/drag ratio improvement of 34% at the operating point produces an estimated 38% $p(\theta)$ increase for blades of $C/R = .10$.

The potential of cyclically manipulated leading edge devices is similarly impressive whether used along or in concert with trailing

---

*Obviously, the applicability of the concept to straight bladed turbines is much greater than to curved bladed turbines.

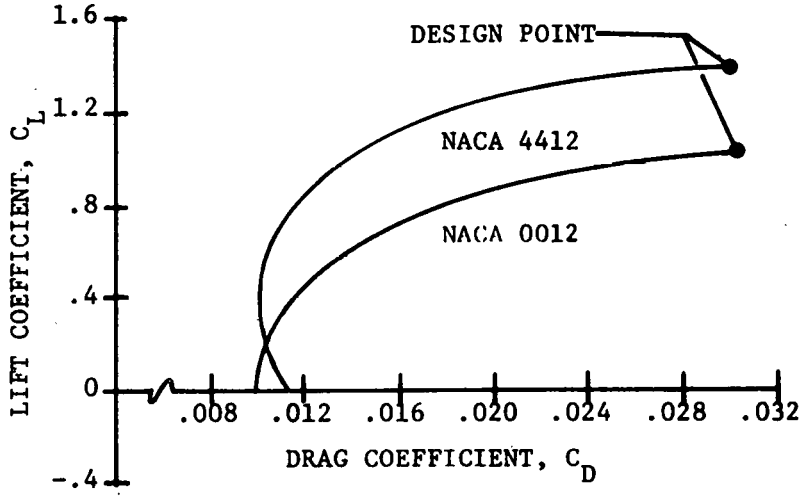

Figure 26. Lift/Drag comparison of cambered and symmetrical airfoils

edge devices. Leading edge devices have the effect of extending the linear range of the lift curve and delaying stall. Thus, higher C_Ls are achieved at higher α. C_L increases of 35% and α_{stall} increases of 60% are typical. Recall that positive torque is proportional to $C_L \sin(\theta-\beta)$ so that a 35% increase in C_L produces a 35% increase in positive torque. Undoubtably, countertorque will also increase since C_D increases with increased C_L. The effect of the increased stall angle is more subtle, since increasing α_{stall} has no direct impact on $(\theta-\beta)$. The increased $(\theta-\beta)$ results from operation at lower TSR which becomes a viable option since the blade stall angle is not exceeded. Of real significance is the fact that a 60% increase in $(\theta-\beta)$ produces approximately 60% increase in $C_L \sin(\theta-\beta)$. The combined effect of a 35% C_L increase and a 60% $(\theta-\beta)$ increase is to more than double $C_L \sin(\theta-\beta)$. The potential performance accruing to blades with leading edge devices seems high. Also mechanical leading edge devices might be designed which would be passive, i.e., require little or no power for operation.

Aerodynamic improvements associated with variable camber may also be achieved by boundary layer and/or circulation control. A major concept contained in the WVU research program is circulation control (cc) by blowing over a rounded trailing edge. Extremely large lift coefficients are developed at virtually all angles of attack, including zero angle. Preliminary analysis [14] shows that even when the power requirements of blowing are deducted, C_p

improvements result. The original cc concept applied to Darrieus turbines involved alternate upper and lower surface blowing as the blades passed through $\theta = 90°$ and $\theta = 270°$. Another interesting possibility is to tailor the blade camber to optimize power extraction either upstream or downstream and then to apply cc on the alternate side. This would simplify the mechanical implementation of cc while at the same time reducing the power requirements for the supply air.

Regardless of how the effects of variable camber are produced, a secondary benefit is a reduction of the TSR at which maximum C_p is achieved, presumably the turbine operating point. Lower TSR are permitted when blade stall angle increases, and lower TSR are dictated when blade drag increases. Reducing the operating TSR implies a reduction in blade angular velocity ω. Much of the turbine structural design is dictated by the centrifugal forces which are proportional to ω^2. Thus, reduced operating TSR makes the structural design criteria less stringent and will certainly reduce costs.

5.5 Summary

A thorough understanding of flow curvature effects is essential to the proper design of Darrieus turbines. Once the mechanisms of virtual aerodynamics are understood, new techniques become available for improving the performance of these machines. Application of cyclically variable camber in combination with cyclically variable

pitch seems particularly promising, although a quantitative assessment of potential performance improvement will require considerably more research.

6. Conclusions

By analysis and experimental verification it has been shown that airfoils in curvilinear flow exhibit aerodynamic lift, drag, and moment characteristics much different than they would in rectilinear flow. The actual geometric airfoils may be transformed to their virtual equivalents by conformal mapping techniques. The virtual airfoils have camber and incidence different from the geometric airfoils, and these properties depend upon α_B, TSR, C/R, and the orbital position, θ. In addition to the effects of virtual camber and incidence, very large radial boundary layer pressure gradients result from flow curvature and act to alter the airfoil characteristics. Sectional data for the virtual airfoils more closely represent the actual aerodynamics than do the sectional data for the geometric airfoils. Within the bounds of the present research, it has not been possible to quantitatively evaluate the centrifugal boundary layer effects.

Virtual aerodynamics are important determinants of Darrieus wind turbine performance. Under most circumstances flow curvature has a detrimental influence on blade aerodynamic efficiency. However, when properly considered, virtual aerodynamics may be used

advantageously to enhance turbine performance. In this regard, the use of variable camber in concert with variable pitch has considerable promise.

7. Continuing Research

In part, the present research has demonstrated that the aerodynamics of Darrieus turbines have not been very well understood. New insights have been developed which provide direction for the continuing research. There appear to be five primary flow phenomena requiring detailed investigation. They are listed here:

1. Virtual aerodynamics
2. Centrifugal effects
3. Reynolds number variation
4. Flow Blockage
5. Flow Unsteadiness

When these are more fully understood, optimization of rotor geometry (n_b, C/R, and b) can proceed more effectively.

As mentioned previously, items number 3, 4, and 5 are more or less independent of the others and will not dictate the choice of airfoil geometry. In other words, they produce second order effects, must be "lived with", and will have approximately the same effect on turbine performance regardless of the choices made on the basis of considerations 1 and 2. If one accepts this argument, then virtual aerodynamics and centrifugal effects are the primary candidates for immediate investigation.

The DOE sponsored research at WVU still has as its primary objective the evaluation of cc airfoils for Darrieus turbine performance improvements. Obviously this goal cannot be achieved without adequate consideration of virtual aerodynamics. Therefore, continuing research will be structured to evaluate cc airfoils with appropriate consideration of virtual aerodynamics. But the research will not include a detailed investigation of virtual aerodynamics and centrifugal effects.*

An experimental program has been formulated which will permit expedient and timely evaluation of cc airfoils. The test apparatus will be an indoor model instrumented to provide lift, drag, and moment data. Indoor testing will greatly simplify the experiments, since the vagaries of the free wind environment will be avoided. At the same time, meaningful data can be obtained (at $V_\infty = 0$) at constant Reynolds number and blade angle of attack. Furthermore, the rotor arm will be adjustable so that a given blade can be tested at various C/R, thus simulating different virtual camber, solidity and Re. Blades previously tested outdoors will be re-used for the indoor tests, thereby permitting at least a qualitative evaluation of Re variation, blockage, and unsteadiness. Wind tunnel tests have already

---

*However, the value of such an investigation should not be underestimated. In fact, the authors believe that such a study would measurably contribute to the understanding of fundamental aerodynamics and advance the technological state of the art of Darrieus turbines. An experimental program has been outlined which systematically investigates the important flow parameters and should isolate the centrifugal and virtual camber effects. This program will be proposed for study at some future date.

been performed on these blades and will provide data for comparison of rectilinear and curvilinear flow aerodynamics. Circulation controlled blades will be fabricated and tested on the indoor machine and data compared to that of the conventional blades.

If favorable cc blade aerodynamics are demonstrated, test results will be used to identify the best configuration for outdoor testing. Follow-on research at the outdoor test site will attempt to verify performance improvements predicted from indoor test results. At the same time, a properly formulated test program will afford the opportunity to investigate the impact of rotor geometry on turbine performance as well as the impact of Re variation, blockage, and flow unsteadiness. It is envisioned that the outdoor test machine will be modified to permit variation of n_b and C/R.

This section presents an outline of the research to be conducted at WVU given the limitations in time, personnel and funding. It is hoped that the material presented in this report will increase the interest of other investigators, and stimulate related research at other institutions.

References

1. Elko, D. G., "Design, Instrumentation, and Calibration of a Vertical Axis Wind Turbine", M.S. Thesis, West Virginia University, Morgantown, WV, May, 1977.

2. Kuhlke, K. D., "Experimental Investigation of the WVU Straight Bladed Darreius Wind Turbine", M.S. Thesis, West Virginia University, Morgantown, WV, May, 1978.

3. Wolfe, W. P., "Analysis of Test Results for the WVU Straight Bladed Darrieus Wind Turbine", M.S. Thesis, West Virginia University, Morgantown, WV, August, 1978.

4. Walters, R. E., et al, "Vertical Axis Wind Turbine Development", ORO/5135-77/5, TR-58, Department of Aerospace Engineering, West Virginia University, July, 1977.

5. Walters, R. E., et al, "Vertical Axis Wind Turbine Experiments and Analysis", ORO/5135-78/1, TR-61, Department of Aerospace Engineering, West Virginia University, May, 1978.

6. Wolfe, W. P., "The Effects of Flow Curvature on the Performance of Darrieus Wind Turbines", 1978 AIAA Middle Atlantic Regional Student Conference, The Pennsylvania State University, State College, PA, April 21-22, 1978.

7. Muraca, R. J., et al, "Theoretical Performance of Cross-Wind Axis Turbines with Results for a Catenary Vertical Axis Configuration", NASA TM X-72662, October, 1975.

8. Kuethe, A. M. and Schetzer, J. D., Foundations of Aerodynamics, John Wiley and Sons, Inc., New York, 1964.

9. Karamcheti, K., Principles of Ideal Fluid Aerodynamics, John Wiley and Sons, Inc., New York, 1966.

10. Ashley, H., "Some Contributions to Aerodynamic Theory for Vertical Axis Wind Turbines', Proceedings of Twelfth Intersociety Energy Conversion Engineering Conference, Washington, D.C., Aug. 28 - Sept. 2, 1977, pp. 1624-1632.

11. Jacobs, E. N., and Sherman, A., "Airfoil Section Characteristics as Affected by Variations of the Reynolds Number, NACA TR 586, Sept. 1937.

12. Abbott, Ira H., and Von Doenhoff, Albert E., Theory of Wing Sections, Dover Publications Inc., New York, 1949.

13. Migliore, P. G., "A Free-Vortex Model with Numerical Solution for the Unsteady Lifting Characteristics of Straight Bladed Darrieus Wind Turbines", Ph.D. Dissertation, West Virginia University, Morgantown, WV May, 1979.

14. Walters, R. E., et al, "Innovative Wind Machines; Executive Summary and Final Report," ERDA/NSF/00367-76/2, Department of Aerospace Engineering, West Virginia University, June, 1976.

APPENDIX A: KINEMATICS

The equation for the local angle of attack along the turbine blade chord is developed with the aid of Figure A1. The present derivation is specialized for the test conditions of the WVU VAWT, that is, a blade of symmetrical airfoil section mounted with its chord perpendicular to the turbine radius arm, $\alpha_B = 90°$. The local relative inflow velocity at any point along the chord is given by

$$V_{R'} = [(\omega R')^2 + V_\infty^2 - 2V_\infty \omega R' \sin\theta']^{\frac{1}{2}} \quad , \tag{A1}$$

where $\theta' = \theta - \Delta\theta$, (A2)

and $\Delta\theta = \arctan\left(\frac{x}{C} \cdot \frac{C}{R}\right)$. (A3)

Noting that $R' = \frac{R}{\cos\Delta\theta}$ (A4)

and defining a local inverse tip speed ratio as

$$\varepsilon' = \frac{V_\infty}{\omega R'} = \varepsilon \cos\Delta\theta \quad , \tag{A5}$$

Equation (A1) may be written as

$$V_{R'} = \omega R'(1 + \varepsilon'^2 - 2\varepsilon' \sin\theta')^{\frac{1}{2}} \quad . \tag{A6}$$

The angle ϕ may be found from the relation

$$\frac{V_\infty}{\sin\phi} = \frac{V_{R'}}{\cos\theta'} \quad . \tag{A7}$$

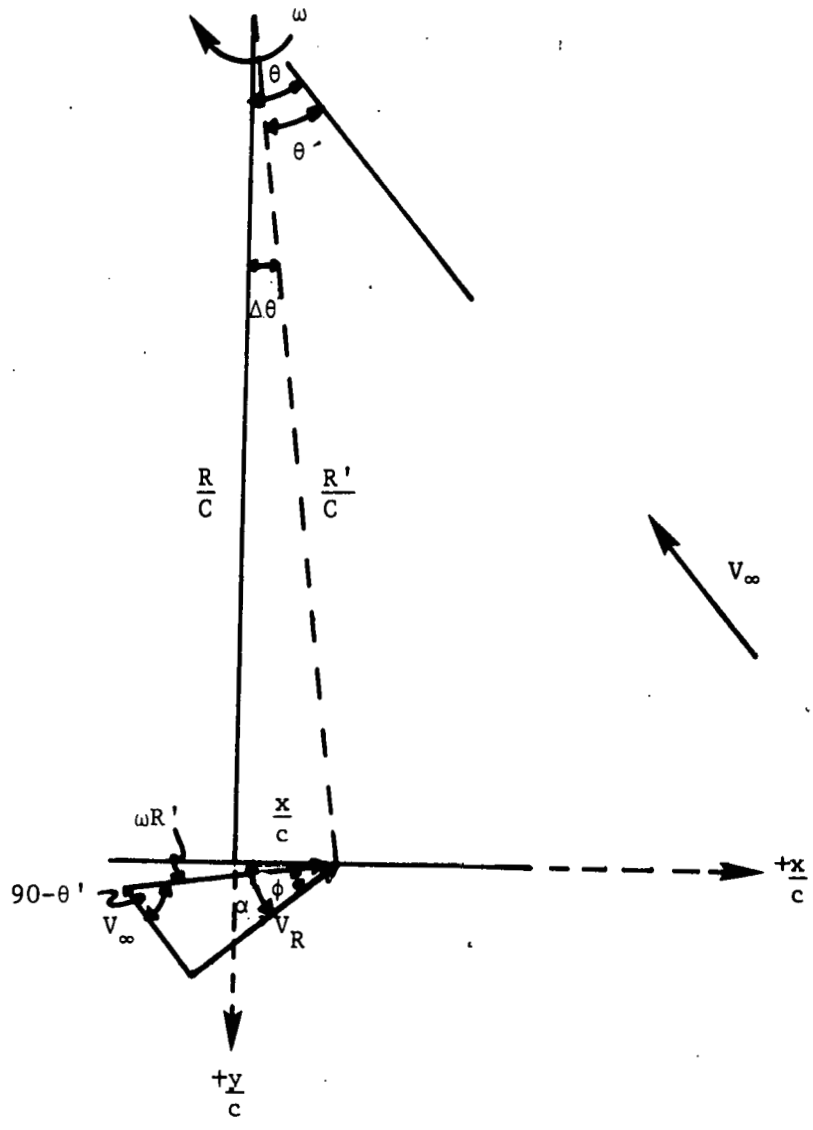

Figure A1. VAWT geometry for determination of local angle of attack

Making the appropriate substitutions gives

$$\phi = \arcsin \frac{\varepsilon' \cos\theta'}{(1 + \varepsilon'^2 - 2\varepsilon' \sin\theta')^{\frac{1}{2}}} \quad , \tag{A8}$$

or in the more convenient arc tangent form,

$$\phi = \arctan \frac{\varepsilon' \cos\theta'}{1 - \varepsilon' \sin\theta'} \quad . \tag{A9}$$

The local angle of attack is

$$\alpha = \phi + \Delta\theta \tag{A10}$$

The equations necessary to calculate the local angle of attack are listed below:

$$\Delta\theta = \arctan \left(\frac{x}{C} \cdot \frac{R}{C}\right) \quad , \tag{A3}$$

$$\theta' = \theta - \Delta\theta \quad , \tag{A2}$$

$$\varepsilon' = \varepsilon \cos \Delta\theta \quad , \tag{A5}$$

$$\theta = \arctan \frac{\varepsilon' \cos\theta'}{1 - \varepsilon' \sin\theta'} \quad , \tag{A9}$$

$$\alpha = \phi + \Delta\theta \quad . \tag{A10}$$

Equations (A1) and (A10) completely define the relative inflow velocity and angle of attack anywhere on the chord, assuming symmetrical airfoils at $\alpha_B = 90°$.

APPENDIX B: TRANSFORMATION EQUATIONS

B.1 Streamline Analysis

Consider a non-inertial (p,q) coordinate system whose origin (0, 0) is at the blade mounting point, and which rotates about the VAWT axis with angular velocity ω. Vector addition of the turbine rotational velocity and the free stream wind gives an expression for the relative inflow velocity.* From Figures B1 and B2 this relative inflow velocity is

$$\vec{V}_R = \{\omega(R + q) - V_\infty \sin\theta\}\,\hat{p} - \{\omega p + V_\infty \cos\theta\}\hat{q} \quad , \tag{B1}$$

where the (^) quantities are unit vectors. Assuming the initial condition $\psi(0, 0) = 0$, the stream function is

$$\psi = \frac{\omega}{2} p^2 + (V_\infty \cos\theta)p + \frac{\omega}{2} q^2 + (\omega R - V_\infty \sin\theta)q. \tag{B2}$$

After manipulation and the introduction of

$$\varepsilon = \frac{V_\infty}{\omega R} \tag{B3}$$

one obtains the relationship

$$\left(\frac{p}{R} + \varepsilon\cos\theta\right)^2 + \left(\frac{q}{R} + 1 - \varepsilon\sin\theta\right)^2 = 1 + \varepsilon^2 - 2\varepsilon \sin\theta + \frac{2\psi}{\omega R^2}, \tag{B4}$$

*It should be noted that the effects of flow blockage are not considered in the analysis. While it is recognized that they are important, for the initial, qualitative study they may be dismissed without compromising the validity of the findings.

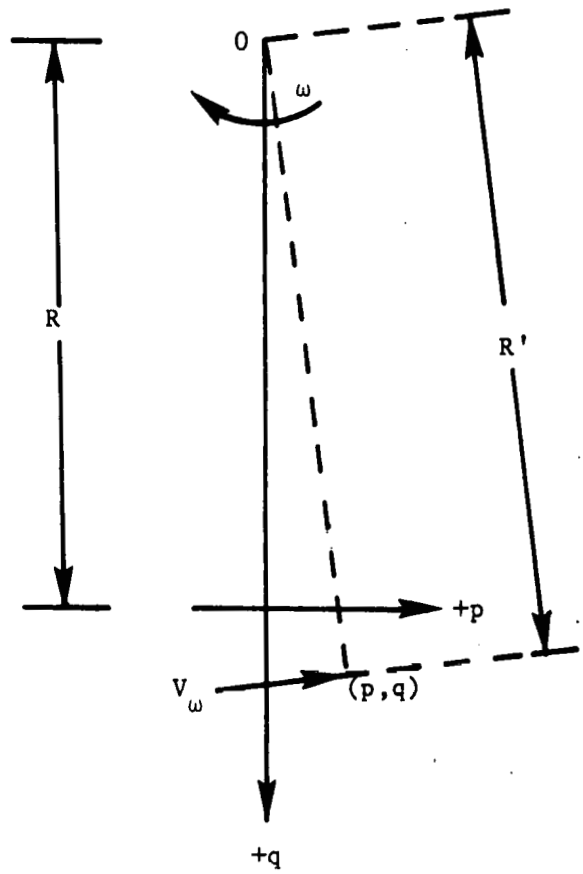

Figure B1. Velocity due to VAWT rotation

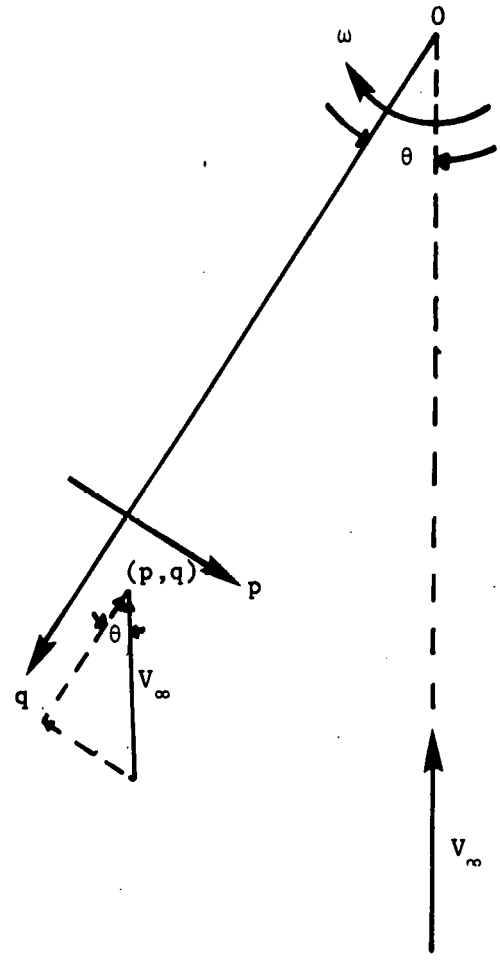

Figure B2. Velocity due to wind

which is the equation for the instantaneous streamlines.

Examination of Equation (B4) shows that the instantaneous streamlines are concentric circles, the origin and radii of which are functions of TSR and θ. Figure B3 shows these streamlines, with their origins at the point O', superimposed over the axes with the center of rotation at point O. All linear displacements have been nondimensionalized by the turbine radius, R. O' appears to rotate counterclockwise about point O at a nondimensional distance, ε.

B.2 Virtual Camber Transformation Equations

The derivations which follow require several different symbols and coordinate systems. To simplify the equations and to clarify the derivations, a system of superscripts and subscripts is used in conjunction with the various alphameric symbols. The superscripts g and v identify quantities which are referred to the geometric and virtual coordinate systems, respectively. The subscripts g, v, and R indicate that quantities have been nondimensionalized by the geometric chord (C^g), the virtual chord (C^v), and the turbine radius (R), respectively.

To transform the circular streamlines into their rectilinear equivalents, a polar coordinate transformation is used. As this type of transformation is conformal, the local angles of attack will be preserved. Using the notation outlined above, from Figure B3

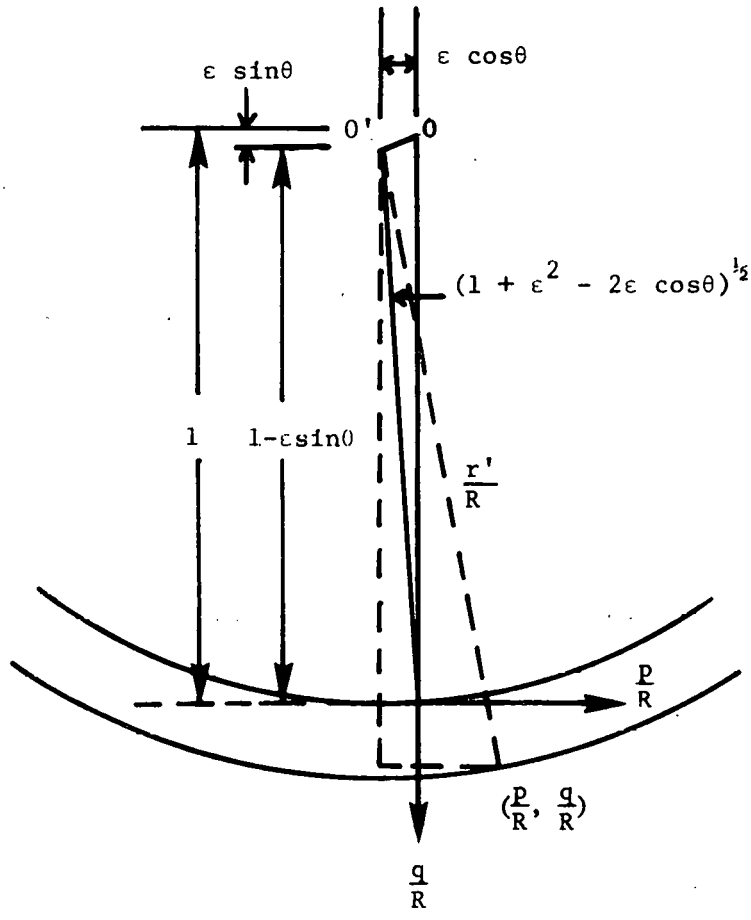

Figure B3. Streamline geometry

and Equation (B4), these transformation equations are

$$q_R^v = \{(p_R^g + \varepsilon\cos\theta)^2 + (q_R^g + 1 - \varepsilon\sin\theta)^2\}^{\frac{1}{2}} \quad , \tag{B5}$$

and

$$p_R^v = \{(p_R^g + \varepsilon\cos\theta)^2 + (q_R^g + 1 - \varepsilon\sin\theta)^2\}^{\frac{1}{2}}.$$

$$\arctan\left[\frac{p_R^g + \varepsilon\cos\theta}{q_R^g + 1 - \sin\theta}\right] \quad . \tag{B6}$$

Equations (B5) and (B6) may be modified so that the origin of the (p^g, q^g) plane transforms into the origin of the (p^v, q^v) plane. Nondimensionalizing the coordinates by the geometric blade chord and defining the symbols

$$\gamma = \varepsilon\cos\theta \quad , \tag{B7}$$

$$\lambda = 1 - \varepsilon\sin\theta \quad , \tag{B8}$$

$$\Gamma = \frac{p_g^g}{Rg} + \gamma \quad , \tag{B9}$$

$$\Lambda = \frac{q_g^g}{Rg} + \lambda \quad , \tag{B10}$$

one obtains

$$\frac{q_g^v}{Rg} = [\Gamma^2 + \Lambda^2]^{\frac{1}{2}} - [\gamma^2 + \lambda^2]^{\frac{1}{2}} \quad , \tag{B11}$$

and

$$\frac{p_g^v}{R_g} = [\Gamma^2 + \Lambda^2]^{\frac{1}{2}} \left[\arctan \frac{\Gamma}{\Lambda} - \arctan \frac{\gamma}{\lambda}\right] . \qquad (B12)$$

Before equations (B11) and(B12) may be used, an additional translation and/or rotation will be required to convert the standard (x_g^g , y_g^g) airfoil coordinates to the (p_g^g , q_g^g) coordinates. The standard NACA coordinate system has the origin at the leading edge, the x/c-axis along the chord line and the y/c-axis 90 degrees counterclockwise. Figure B4 shows a cambered mean line (rotated through an angle α_B) with this standard airfoil coordinate system superimposed over the (p_g^g , q_g^g) coordinate system. From Figure B4, the transformation from (x_g^g , y_g^g) to (p_g^g, q_g^g) gives

$$p_g^g = (x_g^g - k_g^g) \cos\alpha_b + (y_g^g - h_g^g) \sin\alpha_b , \qquad (B13)$$

and

$$q_g^g = (x_g^g - k_g^g) \sin\alpha_b - (y_g^g - h_g^g) \cos\alpha_b . \qquad (B14)$$

The coordinates of the virtual airfoil may also be converted to the standard NACA coordinate system, provided the virtual angle of attack and chord length are known. Applying Equations (B11) and (B12) to the mean line of an airfoil will produce a curve similar to that in Figure B5. From this Figure the virtual angle of attack is

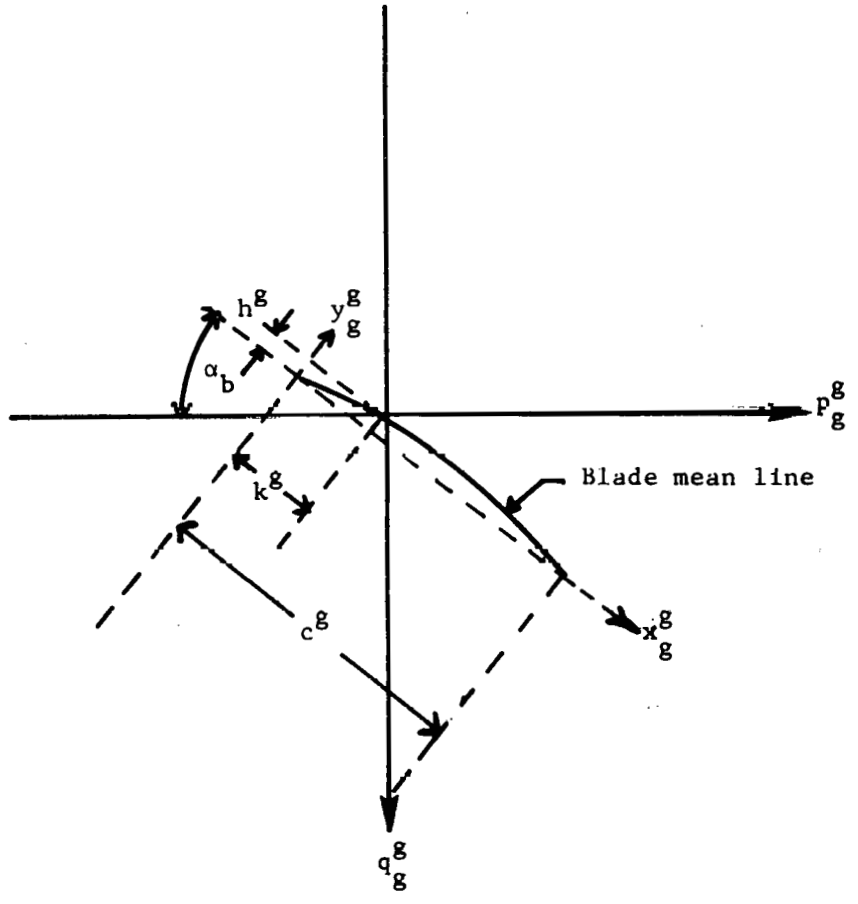

Figure B4. Standard airfoil coordinate system in relation to VAWT coordinate system

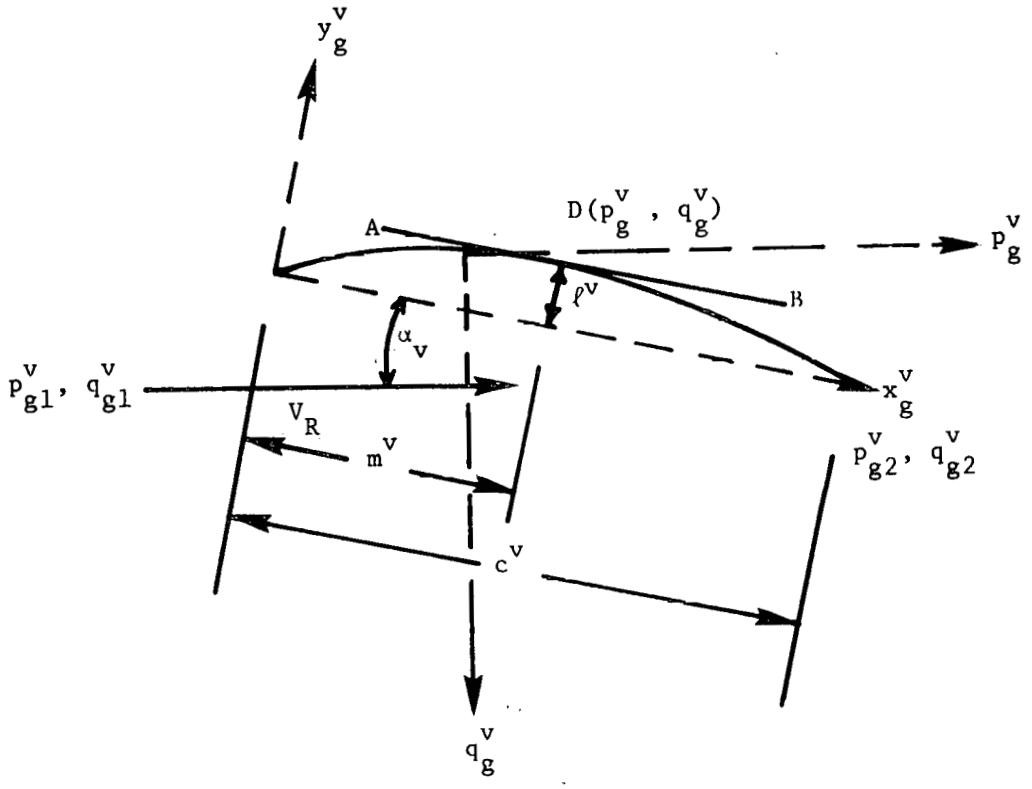

Figure B5. Transformed mean line

$$\alpha_v = \arctan \frac{q^v_{g2} - q^v_{g1}}{p^v_{g2} - p^v_{g1}} \quad , \tag{B15}$$

and the ratio of the virtual chord length to the geometric chord length is

$$\frac{c^v}{c^g} = [(p^v_{g2} - p^v_{g1})^2 + (q^v_{g2} - q^v_{g1})^2]^{\frac{1}{2}} \tag{B16}$$

From Figures B5 and B4, the equations necessary to convert the coordinates from Equations (B11) and (B12) into the standard NACA system are

$$x^v_v = [(p^v_g - p^v_{g1}) \cos\alpha_v + (q^v_g - q^v_{g1}) \sin\alpha_v]\frac{c^g}{c^v} \quad , \tag{B17}$$

and

$$y^v_v = [(p^v_g - p^v_{g1}) \sin\alpha_v - (q^v_g - q^v_{g1}) \cos\alpha_v]\frac{c^g}{c^v} \quad . \tag{B18}$$

B.3 Virtual Airfoil Geometry

Some useful properties of the virtual airfoil may be calculated with the aid of Figure B5. The perpendicular distance, ℓ^v_v, from any point, D, on the transformed mean line may be found by using the formula for the distance from a point to a line, which gives

$$\ell_v^v = [p_g^v(q_{g2}^v - q_{g1}^v) + q_g^v(p_{g1}^v - p_{g2}^v) + p_{g2}^v q_{g1}^v - p_{g1}^v q_{g2}^v] \left(\frac{C^g}{C^v}\right)^2. \quad \text{(B19)}$$

Once the maximum value of ℓ_v^v is known, the chordwise location of the point of minimum camber is

$$m_v^v = \frac{p_g^v - p_{g1}^v}{(C^v/C^g)\cos\alpha_v} - \ell_v^v \tan\alpha_v \quad \text{(B20)}$$

For the case of the symmetrical airfoil, the chordwise location and amount of maximum camber may be calculated directly. From Figure B5 the local angle of attack at the point of maximum camber is α_v. Since the transformation is conformal, this must also be the local angle of attack at the corresponding point in the original airfoil. From Figure B6, this angle is

$$\alpha = \arctan\,[(\Gamma/\Lambda) + \tan\alpha_b]. \quad \text{(B21)}$$

Using the appropriate trigonometric identity, Equation (B21) becomes

$$\alpha = \arctan\left[\frac{\Gamma/\Lambda + \tan\alpha_b}{1 - \Gamma/\Lambda\tan\alpha_b}\right]. \quad \text{(B22)}$$

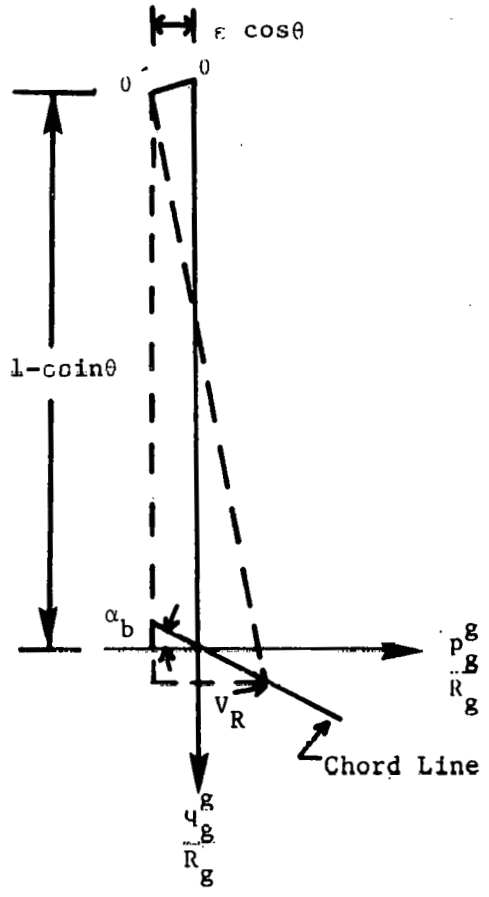

Figure B6. Symmetrical airfoil mean line

Equating (B22) and (B15) and simplifying gives

$$p_g^g = \frac{R_g\left[\frac{q_{g2}^v - q_{g1}^v}{p_{g2}^v - p_{g1}^v}\right](\lambda - \gamma\tan\alpha_b) - \gamma - \lambda\tan\alpha_b}{\sec^2\alpha_b} \quad . \tag{B23}$$

The q_g^g coordinate may be calculated from

$$q_g^g = p_g^g \tan\alpha_b \quad . \tag{B24}$$

The amount and location of maximum camber then follow from Equations (B11), (B12), (B19) and (B20).

B.4 Inverse Virtual Camber Transformation Equations

To develop the inverse transformations, Equations (B13) and (B14) are written in terms of the virtual chord length, and then rearranged to give

$$\frac{p_v^v}{R_v\left[(p_v^g/R_v + \gamma)^2 + (q_v^g/R_v + \lambda)^2\right]^{1/2}} + \arctan\frac{\gamma}{\lambda} = \arctan\frac{p_v^g/R_v + \gamma}{q_v^g/R_v + \lambda} \quad , \tag{B25}$$

and

$$\frac{q_v^v}{R_v} + \left[\gamma^2 + \lambda^2\right]^{1/2} = \left[(p_v^g/R_v + \gamma)^2 + (q_v^g/R_v + \lambda)^2\right]^{1/2} \quad . \tag{B26}$$

Since these equations resulted from a polar coordinate transformation, they may be inverted. The resulting equations are

$$\frac{p_v^g}{R_v} + \gamma = \left[\left(\frac{p_v^g}{R_v} + \gamma\right)^2 + \left(\frac{q_v^g}{R_v} + \lambda\right)^2\right]^{\frac{1}{2}} \sin\left[\arctan \frac{\frac{p_v^g}{R_v} + \gamma}{\frac{q_v^g}{R_v} + \lambda}\right], \qquad \text{(B27)}$$

and

$$\frac{q_v^g}{R_v} + \lambda = \left[\left(\frac{p_v^g}{R_v} + \gamma\right)^2 + \left(\frac{q_v^g}{R_v} + \lambda\right)^2\right]^{\frac{1}{2}} \cos\left[\arctan \frac{\frac{p_v^g}{R_v} + \gamma}{\frac{q_v^g}{R_v} + \lambda}\right]. \qquad \text{(B28)}$$

Making the substitutions from Equations (B25) and (B26) and rearranging gives

$$p_v^g = R_v \left[\frac{q_v^v}{R_v} + (\gamma^2 + \lambda^2)^{\frac{1}{2}}\right] \sin\left[\frac{\frac{p_v^v}{R_v}}{\frac{q_v^v}{R_v} + (\gamma^2 + \lambda^2)^{\frac{1}{2}}} + \arctan\frac{\gamma}{\lambda}\right] - R_v\gamma \ . \qquad \text{(B29)}$$

and

$$q_v^g = R_v\left[\frac{q_v^v}{R_v} + (\gamma^2 + \lambda^2)^{\frac{1}{2}}\right] \cos\left[\frac{\frac{p_v^v}{R_v}}{\frac{q_v^v}{R_v} + (\gamma^2 + \lambda^2)^{\frac{1}{2}}} + \arctan\frac{\gamma}{\lambda}\right] - R_v\lambda \ . \qquad \text{(B30)}$$

As was the case with the virtual camber (direct) transformations, additional manipulations are required to obtain p_v^v and q_v^v from the standard airfoil coordinate systems, and to obtain x_g^g, y_g^g from the p_v^g, q_v^g system.

The resulting inverse transformation equations parallel the direct transformation equations and are

$$p_v^v = (x_v^v - k_v)\cos\alpha_v + (y_v^v - h_v)\sin\alpha_v \quad , \tag{B31}$$

$$q_v^v = (x_v^v - k_v)\sin\alpha_v - (y_v^v - h_v)\cos\alpha_v \quad , \tag{B32}$$

$$\alpha_b = \arctan \frac{q_{v2}^g - q_{v1}^g}{p_{v2}^g - p_{v1}^g} \quad , \tag{B33}$$

$$\frac{C^g}{C^v} = [(p_{v2}^g - p_{v1}^g)^2 + (q_{v2}^g - q_{v1}^g)^2]^{\frac{1}{2}} \quad , \tag{B34}$$

$$x_g^g = [(p_v^g - p_{v1}^g)\cos\alpha_b + (q_v^g - q_{v1}^g)\sin\alpha_b] \frac{C^v}{C^g} \quad , \tag{B35}$$

and $$y_g^g = [(p_v^g - p_{v1}^g)\sin\alpha_b - (q_v^g - q_{v1}^g)\cos\alpha_b] \frac{C^v}{C^g} \quad . \tag{B36}$$

B.5 Geometric Airfoil Characteristics

The geometric blade's mounting angle and chord length are given by Equations (B33) and (B34) respectively. The amount and location of the point of maximum camber may not be calculated directly for the inverse transformation. Instead, the mean line values of y_g^g

from Equations (B36) must be searched for the maximum absolute value to give the amount of camber. The corresponding x_g^g value is the chordwise location of maximum camber.

APPENDIX C: COMPUTER CODES FOR VIRTUAL AIRFOIL TRANSFORMATION

C.1 Introduction

Computer codes have been written which implement the transformation equations of Appendix B. The first program, VIRCAM, utilizes the virtual camber transformation equations to determine the virtual airfoil's geometry given the turbine blade's coordinates and defining parameters. The second program, INVIRCAM, utilizes the inverse virtual camber transformation equations to calculate the desired turbine blade's coordinates and geometric properties given the virtual airfoil's coordinates and appropriate operating parameters.

C.2 VIRCAM

VIRCAM contains 88 lines of FORTRAN IV code and is written for the IBM 360/75-370/145 system. CPU time requirements are 0.57 sec. compile time and 0.71 sec. execution time for one set of operating parameters with an airfoil of 45 coordinate pairs. Data is input to the program through three READ statements. The first READ statement reads an identification index, an alphameric description of the airfoil section, the total number of coordinate pairs, and the number of mean line pairs. The identification index is a one digit number read in column 1 under an I1 format. Zero is used to indicate a symmetrical airfoil. Any positive, single digit integer may be used to indicate a non-symmetrical section. The alphameric description

of the airfoil is read under a 7A4 format beginning in column 2. The number of coordinate pairs is read under an I4 format beginning in column 30. The number of mean line coordinate pairs is read under an I3 format beginning in column 54. The blank spaces after the number of coordinates may be used for comments about the coordinate deck, since they are not read.

The standard NACA designation system was chosen for the airfoil coordinates. The origin is at the leading edge with the x/c axis along the chord line and the y/c axis 90° counter-clockwise. The coordinate arrays are read under a 2F10.0 format, one pair of coordinates per card with x/c preceeding y/c. The mean line coordinates must be first, in sequence from leading to trailing edge. The surface coordinates may be placed in any order.

The remaining read statement reads α_b, θ, TSR, c/R, and the coordinates of the blade's mounting point under an 8F10.0 format. α_b and θ are read in degrees. If a TSR greater than 100 is read, the program uses a TSR of ∞. The values of these variables may be changed for subsequent runs by inserting additional data cards with the appropriate changes. The program terminates when the final card with 999. in the first four columns is encountered. A program listing follows.

The program output consists of a list of input parameters, a table of input and transformed coordinates, and a list of the geometric properties of the transformed airfoil. If a TSR of ∞ was used, the overflow symbol is printed in the TSR space. A sample output plus a list of input and output symbols follows the program listing.

TABLE C-1. VIRCAM INPUT SYMBOLS

Symbol	
ALFBDG	α_b (degrees)
CR	c/R
NCORD	Total number of coordinates pairs
NMEAN	Number of mean line coordinates pairs
SECTN	Description of airfoil
SYM	Symmetrical code: 0 = symmetrical, 1 to 9 = non-symmetrical
THETAD	θ (degrees)
TSR	Tip speed ratio
XC, YC	(x/c, y/c) coordinates of turbine blade; NACA coordinate system
XMOUNT, YMOUNT	Coordinates of mounting point

TABLE C-2. VIRCAM OUTPUT SYMBOLS

Symbol	
ALPHAV	α_v (degrees)
ALPHAB	α_b (degrees)
CHORD RATIO	Ratio of virtual chord length to original chord length
C/R	c/R
L/CC	Amount of maximum camber as fraction of virtual chord
M/CC	Chordwise location of point of maximum camber as fraction of virtual chord
P/C, Q/C	Virtual airfoil coordinates with origin (0, 0) centered at mounting point; nondimensionalized by geometric chord length
THETA	θ (degrees)
TSR	Tip speed ratio
X/C, Y/C	Geometric airfoil coordinates
XX/CC, YY/CC*	Virtual airfoil coordinates with origin (0, 0) at the leading edge; nondimensionalized by virtual chord length

*To obtain (x, y) coordinates, multiply the chord of the geometric airfoil by "CHORD RATIO" and then by (XX/CC, YY/CC).

```
C                              *****VIRCAM*****
C  THIS PROGRAM CALCULATES THE TRANSFORMED COORDINATES FOR A SPECIFIED
C  AIRFOIL USING THE VIRTUAL CAMBER TRANSFORMATION EQUATIONS.
C
C
C
      DIMENSION XC(100), YC(100), PC(100), QC(100), PCCAP(100), QCCAP(100)
     AQ), SECTN (7), PPC(100), QQC(100), XXC(100), YYC(100)
      DATA XC, YC, PC, QC, PCCAP, QCCAP, PPC, QQC, XXC, YYC/1000*0.0/
      REAL LC, MC, LREF
      INTEGER SYM
      PI = 3.141592654
      READ(5,901) SYM, SECTN, NCORD, NMEAN
      READ(5,902) (XC(I),YC(I),I=1,NCORD)
    1 READ(5,903) ALFBDG, THETAD, TSR, CR, XMOUNT, YMOUNT
      IF (ALFBDG.GT.100.) GO TO 900
      WRITE(6,904) SECTN
      WRITE (6,905) XMOUNT, YMOUNT, CR, ALFBDG, THETAD, TSR
      WRITE(6,906)
      ALFB = ALFBDG*PI/180.
      THETA = THETAD*PI/180.
C
C  CALCULATING PROPER VALUE OF EPSILON
C
      IF (TSR.GT.100.) GO TO 3
      EPSLON = 1./TSR
      GO TO 5
    3 EPSLON = 0.0
    5 CONTINUE
C
C  CALCULATING INITIAL TRANSFORMED COORDINATES
C
      DO 10 I = 1,NCORD
      PC(I) = (XC(I)-XMOUNT)*COS(ALFB)+(YC(I)-YMOUNT)*SIN(ALFB)
      QC(I) = (XC(I)-XMOUNT)*SIN(ALFB)-(YC(I)-YMOUNT)*COS(ALFB)
   10 CONTINUE
```

```
      A = EPSLON*COS(THETA)
      B = 1.0 - EPSLON*SIN(THETA)
      C = SQRT(A*A + B*B)
      D = ATAN(A/B)
      DO 20 I = 1,NCORD
      E = PC(I)*CR + A
      F = QC(I) *CR + B
      G = SQRT(E*E + F*F)
      PCCAP(I) = G*(ATAN(E/F) - D)/CR
      QCCAP(I) =(G - C)/CR
 20   CONTINUE
C
C  CALCULATING TRANSFORMED AIRFOIL'S PROPERTIES
C
      ALPHA= ATAN2(QCCAP(NMEAN)-QCCAP(1),PCCAP(NMEAN)-PCCAP(1))
      CHORD=SQRT((PCCAP(NMEAN)-PCCAP(1))**2+(QCCAP(NMEAN)-QCCAP(1))**2)
      IF (SYM.NE.0) GO TO 100
      PRMAX=((QCCAP(NMEAN)-QCCAP(1))/(PCCAP(NMEAN)-PCCAP(1))*(B-A*TAN(AL
     AFB))-A-B*TAN(ALFB))*COS(ALFB)**2
      QRMAX=PRMAX*TAN(ALFB)
      EE = PRMAX + A
      FF = QRMAX + B
      GG = SQRT(EE*EE + FF*FF)
      PCMX = GG*(ATAN(EE/FF) - D)/CR
      QCMX =(GG - C)/CR
      LC=(PCMX*(QCCAP(NMEAN)-QCCAP(1))+QCMX*(PCCAP(1)-PCCAP(NMEAN))+PCCA
     AP(NMEAN)*QCCAP(1)-PCCAP(1)*QCCAP(NMEAN))/CHORD/CHORD
      NC=(PCMX-PCCAP(1))/CHORD/COS(ALPHA)-LC*TAN(ALPHA)
      GO TO 200
 100  LREF = 0.0
      II = 1
      DO 150 I = 1,NMEAN
      LC=(PCCAP(I)*(QCCAP(NMEAN)-QCCAP(1))+QCCAP(I)*(PCCAP(1)-PCCAP(NMEA
     AN))+PCCAP(NMEAN)*QCCAP(1)-PCCAP(1)*QCCAP(NMEAN))/CHORD/CHORD
      IF(LREF.GT.LC) GO TO 150
      LREF = LC
```

```
      LREF = LC
      II = I
  150 CONTINUE
      LC = LREF
      MC=(PCCAP(II)-PCCAP(1))/CHORD/COS(ALPHA)-LREF*TAN(ALPHA)
  200 CONTINUE
C
C  CONVERTING TRANSFORMED COORDINATES TO STANDARD AIRFOIL COORDINATE SYSTEM
C
      DO 210 I = 1, NCORD
      PPC(I) = (PCCAP(I)*COS(ALPHA)+QCCAP(I)*SIN(ALPHA))/CHORD
      QQC(I) = (QCCAP(I)*COS(ALPHA)-PCCAP(I)*SIN(ALPHA))/CHORD
      XXC(I) = PPC(I)-PPC(1)
      YYC(I) = -QQC(I)+QQC(1)
  210 CONTINUE
C
C
      DO 220 I = 1, NMEAN
      WRITE(6,907) XC(I), YC(I), PCCAP(I), QCCAP(I), XXC(I), YYC(I)
  220 CONTINUE
      WRITE(6,909)
      NN = NMEAN + 1
      DO 230 I = NN, NCORD
      WRITE(6,907) XC(I), YC(I), PCCAP(I), QCCAP(I), XXC(I), YYC(I)
  230 CONTINUE
      ALPHAD = ALPHA*180./PI
      WRITE(6,908) ALPHAD, CHORD, LC, MC
      GO TO 1
  900 WRITE(6,910)
      STOP
  901 FORMAT(I1,7A4,I4,20X,I3)
  902 FORMAT(2F10.0)
  903 FORMAT(8F10.0)
  904 FORMAT('1',10(/),38X,'VIRTUAL CAMBER TRANSFORMATION -',7A4)
  905 FORMAT(41X,'MOUNTING POINT: X/C =',F5.2,', Y/C =',F5.2,'; C/R =',F
```

```
      A6.3,/,42X,'ALPHAB =',F6.2,' DEG; THETA =',F5.0,' DEG; TSR =',F5.2)
83    906  FORMAT(///,39X,'X/C',6X,'Y/C',9X,'P/C',6X,'Q/C',8X,'XX/CC',4X,'YY/
      ACC',/)
84    907  FORMAT(37X,3(F6.3,3X,F6.3,6X))
85    908  FORMAT(//,45X,'TRANSFORMED PROPERTIES:  ALPHAV = ',F6.2,' DEG',/,4
      A2X,'CHORD RATIO =',F6.3,'; L/CC =',F7.4,'; M/CC =',F7.4)
86    909  FORMAT(/,56X,'MEAN LINE DATA ABOVE',/,38X,56('*'),/,57X,'AIRFOIL D
      AATA BELOW',/)
87    910  FORMAT('1')
88         END
```

VIRTUAL CAMBER TRANSFORMATION - NACA 0015 AIRFOIL SECTION
MOUNTING POINT: X/C = 0.25, Y/C = 0.00; C/R = 0.260
ALPHAB = 0.00 DEG; THETA = 0. DEG; TSR = 5.50

X/C	Y/C	P/C	Q/C	XX/CC	YY/CC
0.000	0.000	-0.246	-0.037	0.000	0.000
0.100	0.000	-0.148	-0.024	0.097	0.010
0.200	0.000	-0.049	-0.009	0.195	0.018
0.300	0.000	0.049	0.009	0.293	0.024
0.400	0.000	0.148	0.030	0.392	0.027
0.500	0.000	0.246	0.052	0.491	0.028
0.600	0.000	0.345	0.078	0.592	0.027
0.700	0.000	0.444	0.105	0.693	0.023
0.800	0.000	0.543	0.135	0.794	0.017
0.900	0.000	0.642	0.167	0.897	0.010
1.000	0.000	0.742	0.201	1.000	-0.000

MEAN LINE DATA ABOVE

****

AIRFOIL DATA BELOW

0.012	0.024	-0.230	-0.059	0.011	0.025
0.012	-0.024	-0.238	-0.012	0.013	-0.022
0.025	0.033	-0.216	-0.066	0.022	0.035
0.025	-0.033	-0.227	-0.001	0.026	-0.030
0.050	0.044	-0.189	-0.075	0.046	0.049
0.050	-0.044	-0.205	0.013	0.051	-0.038
0.075	0.052	-0.163	-0.079	0.070	0.060
0.075	-0.052	-0.182	0.025	0.076	-0.044
0.100	0.059	-0.137	-0.082	0.094	0.068
0.100	-0.059	-0.158	0.034	0.101	-0.047
0.150	0.067	-0.086	-0.083	0.142	0.081
0.150	-0.067	-0.110	0.049	0.150	-0.051
0.200	0.072	-0.036	-0.079	0.191	0.089
0.200	-0.072	-0.062	0.062	0.199	-0.052
0.250	0.074	0.013	-0.073	0.240	0.094
0.250	-0.074	-0.013	0.073	0.248	-0.052
0.300	0.075	0.063	-0.064	0.289	0.097
0.300	-0.075	0.036	0.083	0.297	-0.050
0.400	0.073	0.161	-0.041	0.388	0.098
0.400	-0.073	0.135	0.100	0.396	-0.044
0.500	0.066	0.258	-0.012	0.488	0.092
0.500	-0.066	0.234	0.117	0.495	-0.036
0.600	0.057	0.355	0.023	0.589	0.082
0.600	-0.057	0.335	0.133	0.595	-0.028
0.700	0.046	0.452	0.061	0.690	0.067
0.700	-0.046	0.435	.149	0.695	-0.021
0.800	0.033	0.549	0.104	0.793	0.049
0.800	-0.033	0.537	0.166	0.796	-0.014
0.900	0.018	0.645	0.150	0.896	0.027
0.900	-0.018	0.639	0.184	0.897	-0.007
0.950	0.010	0.694	0.174	0.948	0.015
0.950	-0.010	0.690	0.193	0.949	-0.004
1.000	0.002	0.742	0.199	1.000	0.001
1.000	-0.002	0.742	0.202	1.000	-0.001

TRANSFORMED PROPERTIES: ALPHAV = 13.53 DEG
CHORD RATIO = 1.016; L/CC = 0.0280; M/CC = 0.4681

C.3 INVIRCAM

INVIRCAM contains 69 lines of FORTRAN IV code and is written for the IBM 360/75-370/145 system. CPU time requirements are 0.40 sec. compile time and 0.77 sec. execution time for one set of parameters with an airfoil of 45 coordinate pairs. All inputs are identical to the VIRCAM program with the exceptions that the SYM index has been eliminated and α_v is input rather than α_b. The output is similar to the VIRCAM output with the exception that the INVIRCAM chord ratio is the inverse of the VIRCAM chord ratio and α_b is output rather than α_v. A list of input and output symbols, program listing, and sample output follow.

TABLE C-3. INVIRCAM INPUT SYMBOLS

Symbol	
ALPHAD	α_v (degrees)
CR	c/R
NCORD	Total number of coordinate pairs
NMEAN	Number of mean line coordinate pairs
SECTN	Description of airfoil
THETAD	θ (degrees)
TSR	Tip speed ratio
XXC, YYC	(x/c, y/c) coordinates of virtual airfoil; NACA coordinate system
XMOUNT, YMOUNT	Coordinate of blade mounting point

TABLE C-4. INVIRCAM OUTPUT SYMBOLS

Symbol	
ALPHAV	α_v (degrees)
ALPHAB	α_b (degrees)
CHORD RATIO	Ratio of turbine chord length to virtual chord length
C/R	c/R
L/C	Amount of maximum camber as fraction of geometric airfoil chord
M/C	Chordwise location of point of maximum camber as fraction of geometric chord
P/C, Q/C	Geometric airfoil coordinate with origin (0, 0) at mounting point; nondimensionalized by virtual chord length
THETA	θ (degrees)
TSR	Tip speed ratio
X/C, Y/C*	Geometric airfoil coordinates
XX/CC, YY/CC	Virtual airfoil coordinates with origin (0, 0) at the leading edge; nondimensionalized by virtual chord length

*To obtain (x, y) coordinates, multiply the chord of the virtual airfoil by "CHORD RATIO" and then by (X/C, Y/C).

```
C                          *****INVIRCAM*****
C  THIS PROGRAM CALCULATES THE COORDINATES FOR A SPECIFIED TRANSFORMED
C  AIRFOIL USING THE INVERSE VIRTUAL CAMBER TRANSFORMATION EQUATIONS
C
C
C
      1       DIMENSION XC(100), YC(100), PC(100), QC(100), PCCAP(100), QCCAP(10
             A0), SECTN(7), PPC(100), QQC(100), XXC(100), YYC(100)
      2       DATA XC, YC, PC, QC, PCCAP, QCCAP, PPC, QQC, XXC, YYC/1000*0.0/
      3       REAL LC, MC
      4       PI = 3.141592654
      5       READ(5,901) SECTN, NCORD, NMEAN
      6       READ(5,902) (XXC(I), YYC(I), I = 1,NCORD)
      7    1  READ(5,903) ALPHAV, THETAD, TSR, CR, XMOUNT, YMOUNT
      8       IF(ALPHAV.GT.100.) GO TO 900
      9       WRITE(6,904) SECTN
     10       WRITE(6,905) XMOUNT, YMOUNT, CR, ALPHAV, THETAD, TSR
     11       WRITE(6,906)
     12       ALPHA = ALPHAV*PI/180.
     13       THETA = THETAD*PI/180.
C
C  CALCULATING PROPER VALUE OF EPSILON
C
     14       IF(TSR.GT.100.) GO TO 3
     15       EPSLON = 1./TSR
     16       GO TO 5
     17    3  EPSLON = 0.0
     18    5  CONTINUE
C
C  CALCULATING INITIAL TRANSFORMED COORDINATES
C
     19       DO 10 I = 1,NCORD
     20       PCCAP(I) = (XXC(I)-XMOUNT)*COS(ALPHA)+(YYC(I)-YMOUNT)*SIN(ALPHA)
     21       QCCAP(I) = (XXC(I)-XMOUNT)*SIN(ALPHA)-(YYC(I)-YMOUNT)*COS(ALPHA)
     22   10  CONTINUE
     23       A = EPSLON*COS(THETA)
```

```
      B = 1.0 - EPSLON*SIN(THETA)
      C = SQRT(A*A + B*B)
      D = ATAN(A/B)
      DO 20 I = 1,NCORD
      E = OCCAP(I)*CR + C
      F = PCCAP(I)*CR/E  + D
      PC(I) = (E*SIN(F) - A)/CR
      QC(I) = (E*COS(F) - B)/CR
   20 CONTINUE
C
C  CONVERTING TRANSFORMED COORDINATES TO STANDARD AIRFOIL COORDINATE SYSTEM
C
      ALFB = ATAN2(QC(NMEAN)-QC(1),PC(NMEAN)-PC(1))
      CHORD = SQRT((PC(NMEAN)-PC(1))**2+(QC(NMEAN)-QC(1))**2)
      DO 30 I = 1,NCORD
      PPC(I) = (PC(I)*COS(ALFB)+QC(I)*SIN(ALFB))/CHORD
      QQC(I) = (QC(I)*COS(ALFB)-PC(I)*SIN(ALFB))/CHORD
      XC(I) = PPC(I) - PPC(1)
      YC(I) = -QQC(I) + QQC(1)
   30 CONTINUE
C
C  CALCULATING TRANSFORMED AIRFOIL'S PROPERTIES
C
      YCREF = 0.0
      II = 1
      DO 40 I = 1,NMEAN
      WRITE(6,907) XXC(I), YYC(I), PC(I), QC(I), XC(I), YC(I)
      IF(YCREF.GT.ABS(YC(I)))GO TO 40
      II = I
      YCREF = YC(I)
   40 CONTINUE
C
C
      WRITE(6,909)
      NN = NMEAN + 1
```

```
      DO 50 I = NN, NCORD
      WRITE(6,907) XXC(I), YYC(I), PC(I), QC(I), XC(I), YC(I)
50    CONTINUE
      ALFBDG = ALFB*180./PI
      WRITE(6,908) ALFBDG, CHORD, YC(II), XC(II)
      GO TO 1
900   WRITE(6,910)
      STOP
901   FORMAT(7A4,1X,I4,20X,I3)
902   FORMAT(2F10.0)
903   FORMAT(8F10.0)
904   FORMAT('1',10(/),34X,'INVERSE VIRTUAL CAMBER TRANSFORMATION -',7A4
     A)
905   FORMAT(41X,'MOUNTING POINT: X/C =',F5.2,', Y/C =',F5.2,'; C/R =',F
     A6.3,/,42X,'ALPHAV =',F6.2,' DEG; THETA =',F5.0,' DEG; TSR =',F5.2)
906   FORMAT(///,38X,'XX/CC',4X,'YY/CC',8X,'P/C',6X,'Q/C',9X,'X/C',6X,'Y
     A/C',/)
907   FORMAT(37X,3(F6.3,3X,F6.3,6X))
908   FORMAT(//,45X,'TRANSFORMED PROPERTIES:  ALPHAB = ',F6.2,' DEG',/,4
     A2X,'CHORD RATIO =',F6.3,'; L/C =',F7.4,'; M/C =',F7.4)
909   FORMAT(/,56X,'MEAN LINE DATA ABOVE',/,38X,56('*'),/,56X,'AIRFOIL D
     AATA BELOW',/)
910   FORMAT('1')
      END
```

INVERSE VIRTUAL CAMBER TRANSFORMATION - INVERSE OF NACA 0015
MOUNTING POINT: X/C = 0.25, Y/C = 0.00; C/R = 0.260
ALPHAV = 3.66 DEG; THETA = 0. DEG; TSR =*****

XX/CC	YY/CC	P/C	Q/C	X/C	Y/C
0.000	0.000	-0.249	-0.024	0.000	0.000
0.099	0.012	-0.150	-0.025	0.100	0.000
0.198	0.020	-0.051	-0.024	0.200	-0.000
0.297	0.027	0.049	-0.024	0.300	0.000
0.396	0.031	0.148	-0.024	0.400	0.000
0.496	0.032	0.247	-0.024	0.500	0.000
0.596	0.030	0.347	-0.024	0.600	-0.000
0.696	0.027	0.446	-0.024	0.700	0.000
0.797	0.020	0.545	-0.024	0.800	-0.000
0.898	0.011	0.644	-0.024	0.900	-0.000
1.000	0.000	0.744	-0.024	1.000	0.000

MEAN LINE DATA ABOVE

****

AIRFOIL DATA BELOW

0.011	0.025	-0.237	-0.048	0.013	0.024
0.014	-0.022	-0.237	-0.000	0.013	-0.024
0.023	0.035	-0.224	-0.056	0.025	0.032
0.027	-0.029	-0.224	0.008	0.025	-0.032
0.047	0.050	-0.199	-0.068	0.050	0.044
0.052	-0.038	-0.200	0.020	0.050	-0.044
0.071	0.061	-0.175	-0.076	0.075	0.053
0.078	-0.043	-0.174	0.028	0.076	-0.052
0.095	0.069	-0.150	-0.082	0.100	0.058
0.103	-0.046	-0.150	0.034	0.100	-0.058
0.144	0.082	-0.101	-0.090	0.150	0.066
0.153	-0.050	-0.100	0.042	0.150	-0.067
0.193	0.091	-0.051	-0.095	0.200	0.071
0.202	-0.051	-0.051	0.047	0.200	-0.072
0.243	0.098	-0.001	-0.098	0.250	0.075
0.252	-0.050	-0.001	.050	0.250	-0.075
0.292	0.101	0.048	-0.098	0.300	0.075
0.302	-0.048	0.049	0.051	0.300	-0.075
0.392	0.102	0.148	-0.096	0.400	0.072
0.401	-0.041	0.148	.048	0.400	-0.072
0.492	0.097	0.248	-0.089	0.500	0.066
0.500	-0.034	0.247	0.042	0.500	-0.066
0.592	0.087	0.346	-0.081	0.600	0.057
0.599	-0.026	0.346	0.033	0.600	-0.057
0.693	0.072	0.446	-0.070	0.700	0.046
0.699	-0.019	0.446	0.022	0.700	-0.046
0.795	0.052	0.545	-0.056	0.800	0.032
0.799	-0.012	0.545	0.009	0.800	-0.033
0.897	0.029	0.644	-0.042	0.900	0.018
0.899	-0.006	0.644	-0.006	0.900	-0.018
0.948	0.016	0.694	-0.034	0.950	0.010
0.950	-0.004	0.695	-0.014	0.950	-0.010
1.000	0.002	0.744	-0.026	1.000	0.002
1.000	-0.002	0.744	-0.022	1.000	-0.002

TRANSFORMED PROPERTIES: ALPHAB = 0.01 DEG
CHORD RATIO = 0.993; L/C = 0.0005; M/C = 0.1001

☆U.S. GOVERNMENT PRINTING OFFICE: 1980-740-145/699